Universidade Estadual de Campinas
Instituto de Física Gleb Wataghin

Danilo Rodrigues de Assis Elias

Exploration of phase behavior of classical spin systems using machine learning

Exploração de comportamentos de fase em modelos de spin clássicos utilizando aprendizado de máquina

Campinas
2023

Danilo Rodrigues de Assis Elias

Exploration of phase behavior of classical spin systems using machine learning”

Exploração de comportamentos de fase em modelos de spin clássicos utilizando aprendizado de máquina

Thesis presented to the Institute of Physics Gleb Wataghin of the University of Campinas in partial fulfillment of the requirements for the degree of Master in Physics, in the area of Applied Physics.
Tese apresentada ao Instituto de Física Gleb Wataghin da Universidade de Campinas como requisito parcial para a obtenção do título de Mestre em Física, na área de Física Aplicada.

Supervisor/Orientador: Prof. Dr. Maurice de Koning. Este trabalho corresponde à versão final da tese defendida pelo aluno Danilo Rodrigues de Assis Elias e orientada por Maurice de Koning

Campinas
2023

Ficha catalográfica
Universidade Estadual de Campinas
Biblioteca do Instituto de Física Gleb Wataghin
Lucimeire de Oliveira Silva da Rocha - CRB 8/9174

EL42e

Elias, Danilo Rodrigues de Assis, 1997-
Exploration of phase behavior of classical spin systems using machine learning / Danilo Rodrigues de Assis Elias. – Campinas, SP : [s.n.], 2023.

Orientador: Maurice de Koning.
Dissertação (mestrado) – Universidade Estadual de Campinas, Instituto de Física Gleb Wataghin.

1. Transformações de fase (Física estatística). 2. Aprendizado de máquina. 3. Sistemas de spin. 4. Frustração. I. Koning, Maurice de, 1969-. II. Universidade Estadual de Campinas. Instituto de Física Gleb Wataghin. III. Título.

Informações Complementares

Título em outro idioma: Exploração de comportamentos de fase em modelos de spin clássicos utilizando aprendizado de máquina
Palavras-chave em inglês:
Phase transformations (Statistical physics)
Machine learning
Spin systems
Frustration
Área de concentração: Física Aplicada
Titulação: Mestre em Física
Banca examinadora:
Maurice de Koning [Orientador]
Eduardo Miranda
José Abel Hoyos Neto
Data de defesa: 24-03-2023
Programa de Pós-Graduação: Física

Identificação e informações acadêmicas do(a) aluno(a)
- ORCID do autor: https://orcid.org/0000-0002-0752-1955
- Currículo Lattes do autor: http://lattes.cnpq.br/7002884321412301

MEMBROS DA COMISSÃO EXAMINADORA DA DISSERTAÇÃO DE MESTRADO DO ALUNO DANILO RODRIGUES DE ASSIS ELIAS - RA 166389 APRESENTADA E APROVADA AO INSTITUTO DE FÍSICA GLEB WATAGHIN, DA UNIVERSIDADE ESTADUAL DE CAMPINAS, EM 24/03/2023.

COMISSÃO JULGADORA:

- Prof. Dr. Maurice de Koning – Presidente e orientador (IFGW/UNICAMP)

- Prof. Dr. Eduardo Miranda (IFGW/UNICAMP)

- Dr. Jose Abel Hoyos Neto (Instituto de Física São Carlos - USP)

OBS.: Ata da defesa com as respectivas assinaturas dos membros encontra-se no SIGA/Sistema de Fluxo de Dissertação/Tese e na Secretaria do Programa da Unidade.

CAMPINAS

2023

Abstract

We apply a set of machine-learning (ML) techniques for the global exploration of the phase diagrams of two frustrated 2D Ising models with competing interactions. Based on raw Monte Carlo spin configurations generated for random system parameters, we apply principal-component analysis (PCA) and auto-encoders to achieve dimensionality reduction, followed by clustering using the DBSCAN method and a support-vector machine classifier to construct the transition lines between the distinct phases in both models. The results are in very good agreement with available exact solutions, with the auto-encoders leading to quantitatively superior estimates, even for a data set containing only 1400 spin configurations. In addition, the results suggest the existence of a relationship between the structure of the optimized auto-encoder latent space and physical characteristics of both systems. This indicates that the employed approach can be useful in perceiving fundamental properties of physical systems in situations where a priori theoretical insight is unavailable.

Resumo

Nós aplicamos um conjunto de técnicas de aprendizado de máquina para a exploração global de diagramas de fase de dois modelos de Ising frustrados com competição entre interações. Baseado em configurações puras geradas por Monte Carlo com parametros aleatórios do sistema nós aplicamos Análise de componente principal (PCA) e auto-encoders para atingir redução de dimensionalidade, seguido de clusterização utilizando o método DBSCAN e uma máquina de vetores suporte como classificador para gerar as linhas de transição entre as fases distintas em ambos os modelos. Os resultados concordam com soluções analíticas disponíveis, com o autoencoder levando a melhores estimativas quantitativas, mesmo para um conjunto de dados consistindo de apens 1400 configurações de spin. Além disso, os resultados sugerem a existência de uma relação entre a estrutura do espaço latente otimizado do auto-encoder e características físicas dos sistemas. Isso indica que a abordagem utilizada pode ser útil para descobrir propriedades fundamentais do sistema em contextos em que entendimento teórico se enontra indisponível.

Contents

Chapter 1

Introduction

Artficial intelligence, AI, is being developed arguably since the time of Alan Turing himself. Theoretical developments did not cease during the decades past, and with the increase of computational power in the 2000's concrete realizations of the theory started to be implemented.

Artificial intelligence as we have developed it is nothing but pattern recognition taken to the extreme. In the last decade the use of graphical processing units, GPU's, allowed us to make AI part of our day to day lives in recomendation algorithms, for example.

It would not be long before physicists took notice of the pattern recognition power of AI and tried to take advantage of it to solve physical problems. As a result, in the past 5 years the field of Machine Learning, ML, applied to physics has exploded into life. It is now a very active area of research with even specialized journals.

The objective of my masters studies was to analyze and interpret phase transitions and physical behavior purely from ML analysis. Interpreting the results requires a great understanding of phase transitions, so I took on the task of studying them as thoroughly as possible before actually performing the analysis. The present work is a full account of my journey.

It is relevant to explain my goal in writing and how this work is organized. In my personal opinion, the content of this thesis is difficult, very difficult. I recall trying to read some of the standard references in phase transitions and feeling absolutely daunted.

It is rare to find a reference suitable for begginers which is not shallow. Conversely, it is rare to find an advanced reference inteligible to beginners. I try to bridge the two here.

You could see this thesis as a case study of Ising models, starting from their deffinition and motivation, then moving on to two different monte carlo approaches. First I deduce the metropolis criterium, then I lead the way from the single spin flip algorithm to the cluster approach by qualitative examples of critical slowing down. Having understood what the problem is and how to solve it, I formally analyze the different approaches by means of correlation functions.

Prior to using simulations to extract the thermodynamics of the system, I try to convey how thermodynamics and statistical mechanics are at the heart of these methods. Having done that I proceed to measure physical quantities from our samples, displaying the full power of computational experiments.

An interlude occurs in which we discuss somewhat in depth the renormalization group approach by Wilson to further our understanding of criticality. Here I favour conceptual clarity over of mathematical rigour. By no means it is a full account of the renormalization group theory, but it allows us to derive the renormalization group flow, power law behavior and scaling relations, culminating in my favorite concept in all of physics: universality. Next I make use of finite size scaling to compute all of the critical exponents in the Ising universality class.

At this point we have done a thorough analysis of the phase transition in the standard Ising model and present more complex idealizations of magnets, which can account for a wider variety of behaviors. These contain the effects of frustration, giving rise to antiferromagnetic, ferromagnetic and paramagnetic phases with macroscopically degenerate, yet ordered, ground states. Appart from that, the models presented can be mapped into a spin glass at one particular point of the phase diagram

These idealizations are analytically solvable, allowing for a full understanding of their thermodynamics. Frustrated magnetism is notoriously difficult to study, theoretically and computationally, so the availability of solutions is both rare and very invaluable to understand the physics of real materials. I solve the ground state for one of the models using transfer matrix techniques, discuss its implications and finally relate them to experimental studies.

These frustrated models can be simulated with the techniques developed in chapter

two and we could analyze their phase transitions via finite size scaling as well. Now, the work developed in my masters asks a different question. Suppose we know nothing but a systems hamiltonian and no prior theoretical insight is available. Can we develop a Machine Learning procedure to analyze monte carlo data and learn about the existence of phases, phase transitions, order, entropy, etc ? The answer is in our published article at the end of this document.

Chapter 2

Monte Carlo and the Ising Model

This chapter relies heavily on refs [1],[2],[3],[4] and [5].

The Ising Model [6] intends to represent an ideal ferromagnet formed by lattices of interacting spins with two well-defined orientations: up (+1) and down (-1). This is a simplification of the magnetic dipole moments of the atomic spins. The energy of the System is described by a Hamiltonian in the form:

$$H(\sigma_i) = -J \sum_{\langle i,j \rangle} \sigma_i \sigma_j \tag{2.1}$$

where J is a positive constant with energy dimensions and the notation $\langle i, j \rangle$ implies that only neighboring spins on the network interact [6]. In this case, J is analogous to an exchange interaction which favours energetically that neighbouring spins should be aligned. The model captures the situation of total magnetization (aligned spins) and null magnetization (disordered spins). The importance of the Ising Model is historical, it had been decades since the model was proposed in 1925 by Lenz to his PhD student, Ising, [7] until the scientific community realized that it in fact described an ideal ferromagnet and that it a second order phase transition at non-zero temperature, Ising himself neglected it [7]. No conclusion was reached until Onsager [8] proposed his solution in 1944. From there, the model gained fame and generated a stir among physicists for being simple and describing a range of phase transition phenomena. It is perhaps the most exhaustively studied in all of statistical mechanics.

Other than physics, there are applications in many systems where a variable, in our case spin, can be represented by two well-defined states, for example, belonging to one or another species in biology [7].

The Model can be studied for cases of different dimensions. In the case of dimension 1 (a horizontal chain of spins, for example) the analytical expression for the free energy, found by Ising [6], has no discontinuities in its derivatives at non-zero temperature, so there is no identification of a phase transition. In 2D (a checker grid, as in the case of this project) the expression for the energy [8] presents discontinuity in its second derivative, identifying a second-order (magnetic or continuous) phase transition that can be observed experimentally by the Curie point of ferromagnetic materials.

I studied the . This chapter is a summary of algorithms developed for the Ising model with their results. First we present the single spin-flip algorithm and then the cluster algorithm. Their respective efficiency in the vicinity of the phase transition is extensively analysed and we obtain the critical exponents of the 2D Ising Model to fully characterize the phase transition.

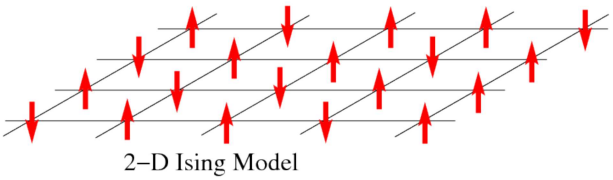

Figure 2.1: Illustration for the Ising Model used in this project. Adapted from [9]

Figure 2.2: Nickel ring reaching its Curie Point and giving in to gravity. Adapted from [10]

2.1 Single Spin Flip Algorithm

Monte Carlo in a nutshell is a method of discovering how a model would behave in an experiment if it was present in nature. It is actually to perform experiments with models, we are free to vary external parameters such as temperature and rate of cooling and observe the systems response. For instance, a *real* ferromagnetic material when when cooled too rapidly from high temperatures will not gain any net magnetization, for there is not enough time for the system to find the global minimum. Instead, it will be in a local minimum. This situation is exactly depicted by monte carlo algorithms for the Ising Model.

Now, to the method of experimenting itself, the single-spin flip algorithm. The interaction with a heatbath generates thermal fluctuations in the system which may overcome the local energy barrier between neighbouring spins and flip the one in the middle. We model this by randomly choosing a lattice site and proposing a flip. This will be accepted if it matches a condition, which we discuss in the next paragraph. Before continuing, notice that this process correspond to a random walk in state space, and given a temperature we can tell whether we are likely to move or not to a new state following the boltzmann distribution. The intention of Monte Carlo algorithms is to sample as much as possible of the state space with the *correct* local density so that we can take ensemble averages of the sampling process. This is sometimes referred to as Importance Sampling.

We will deduce the metropolis acceptance criterium first, necessary for both dynamics (single-spin and cluster) presented in this section.

From the laws of basic probability, we know that the sum of the probabilities of being in one state and transitioning to any other accessible state must be 1

$$\sum_{i}^{n} P\left(a \to i\right) = 1, i \leq a \leq n \tag{2.2}$$

We also know that the probability of being in a certain state a is given by

$$\pi_a = \sum_{i}^{n} \pi_i P\left(i \to a\right) \tag{2.3}$$

We combine both to arrive at the Global Balance Condition (GBC) [1] [2]

$$\sum_{i}^{n} \pi_a P\left(a \to i\right) = \sum_{i}^{n} \pi_i P\left(i \to a\right) \tag{2.4}$$

which must be satisfied by any process. Hence, it becomes a necessary and sufficient condition for the output of the algorithm to represent a distribution. One of the ways to satisfy the GBC is the Detailed Balance Condition (DBC), which consists of matching the sums term by term [1] [2] .

$$\pi_a P\left(a \to i\right) = \pi_i P\left(i \to a\right) \tag{2.5}$$

This equality tells us that the probabilities of being in one configuration and going to another and vice versa must be equal. Bearing this in mind, we must deal with configuration change attempts and in the case of an unlikely move, rejections, so that we are not forced to disregard possible attempts. That is to say, we respect a local probability density to build the whole profile via a weighted random walk. This is the core idea of the Metropolis acceptance criterium. Let's break down the transition probabilities into the product between the probability of a move towards the new state being proposed and the probability of it being accepted:

$$P\left(a \to i\right) = g\left(a \to i\right) A\left(a \to i\right) \tag{2.6}$$

relating the last two equations we arrive at the Metropolis acceptance criterium [1] [2]

$$A(a \to i) = min\left(1, \frac{\pi_i g\left(a \to i\right)}{\pi_a g\left(i \to a\right)}\right) \tag{2.7}$$

which tells us that if we are in a higher probability configuration we must always stay, otherwise we must leave according to the ratio between the probabilities of being at the end and the initial state. The criterium respects the DBC so we build the distribution of interest.

Monte Carlo is a class of algorithms that samples distributions, and this feature suits it for the study of statistical mechanics. In the case of the Ising Model, we would like to sample the state distribution of the canonical ensemble.

$$P = \frac{\exp^{\frac{-E}{kt}}}{Z} \tag{2.8}$$

We must first define what a sampled event will be: a spin inversion. This inversion causes a variation in the energy of the system, this will be our transit between configurations (states of different energies) [1] [2]. Now we can apply the DBC and the Metropolis acceptance criterium:

$$A(a \to i) = min\left(1, \frac{\pi_i g\,(i \to a)}{\pi_a g\,(a \to i)}\right) \tag{2.9}$$

Taking into account that we randomly choose a spin to invert, the probabilities that any two moves (inversions) are proposed are equal, simplifying the criterium to:

$$A(a \to i) = min\left(1, \frac{\pi_i}{\pi_a}\right) \tag{2.10}$$

In this case π_n indicates the probability of being in a state with energy E_n. The expression we should use is that of the canonical ensemble:

$$A(a \to i) = min\left(1, \frac{(1/Z)\exp(-\beta E_i)}{(1/Z)\exp(-\beta E_a)}\right) \tag{2.11}$$

now we can build the desired distribution. It is worth noting that we will accept the spin inversion with probability 1 if $\Delta E < 0$, this is a coupling effect of neighboring spins; if possible they try to align [7].

For the calculations of thermodynamic quantities to be carried out, we need to give an initial condition to the system, which, in our case, consisted of the ground state of the model. This is the case at a temperature close to zero, so in order to calculate the energy, for example, at a given temperature, enough Monte Carlo trials (measurements in sweeps) must be carried out for the system to reach equilibrium with the bath [2]. This process works correctly and efficiently up to and after the critical temperature, where fluctuations take over. In this region the system configuration changes drastically; this is where our order parameter (spin magnetization) goes from 1 to zero continuously. This indicates, roughly, that we have gone from the state where all spins are aligned to one of total disorder. Within the dynamics of the single flip algorithm we then have to change the orientation of the spins, one by one. It can then be seen that the equilibration time grows dramatically at the critical temperature with respect to previous values, as seen in the figures.

A fact that should be noted is that we only identify the phase transition in the thermodynamic limit [8], since the partition function of this system is a sum of analytical

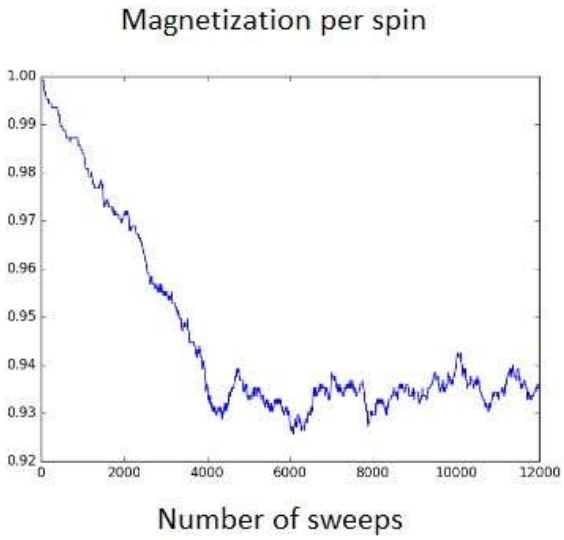

Figure 2.3: Equilibration for T=2 on an edge 50 takes about 4000 sweeps

terms only an infinite sum could be non analytic. So we must have lattices as large as possible, increasing the number of spins. A serious problem then arises in our dynamics: with a greater number of spins, even more Monte Carlo trials are necessary for equilibration, limiting the the size and making it difficult to identify the phase transition. Keeping in mind the physics of the system, we come to the conclusion that the random walk through phase space is extremely slow in the critical region making it very difficult to acquire uncorrelated samples for meaningful averages. This phenomenon, known as *critical slowing down* [1] [2], makes the computational cost of the single flip algorithm very high, although the final result would be correct. It is worth noting that this is not a problem of optimization, or of having access to more CPU's to perform the calculations; it is an inherent feature of the phase transition. This fact motivated the development of other Monte Carlo dynamics for the Ising Model.

2.2 Wolff Cluster Algorithm

The dynamics presented here, developed in 1989 by Ulli Wolff [3], deserves special attention for it represented a revolution in numerical methods in statistical mechanics.

To solve the *critical slowing down*, we would like to "take larger steps" in state space with each Monte Carlo move. This is translated into changing the orientation of several spins at once. To do so, we will choose a spin at random and add a neighbor with

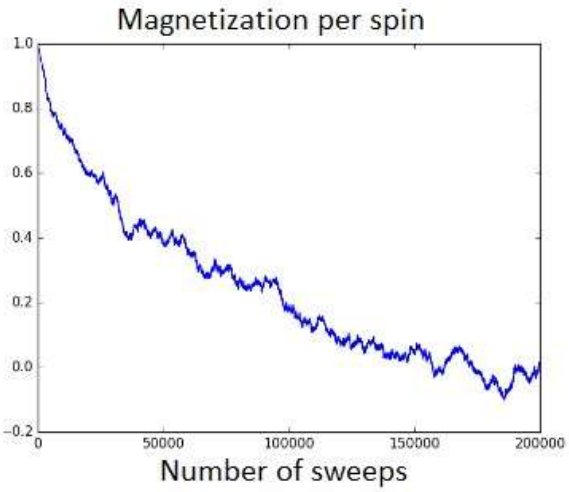

Figure 2.4: Equilibration for T=2.7 on an edge 50 takes over 200000 sweeps. Note that the identified "critical" temperature is offset from the theoretical value due to algorithm and edge limitations

the same orientation to form a cluster with probability p [1]. We must check all neighbors of the initial spin and repeat the procedure for the added spins, taking care not to check the spin from which this new one was added. At some point no new spin will enter the cluster, ceasing its construction [2].

We must now develop a criterion to be able to invert the cluster as a whole at once. Looking at figure 2.5, which shows a cluster in the final stage of construction and the inverted state, we can apply the detailed balance condition:

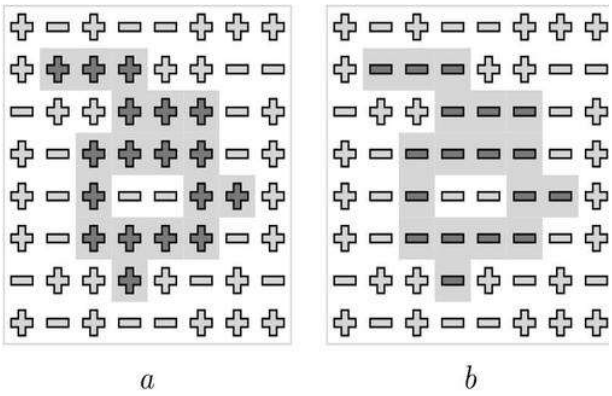

Figure 2.5: Cluster in final stage of construction. Source: [1]

$$\pi_a P\left(a \to b\right) = \pi_b P\left(b \to a\right) \tag{2.12}$$

where $P\left(a \to b\right)$, as before, will be broken down into the probability of a move in that

direction being proposed (probability of this cluster being built) times the probability of it being accepted:

$$P\left(a \to b\right) = p_{acc}\left(a \to b\right) A\left(a \to b\right) \tag{2.13}$$

substituting in eq.12 we will have:

$$\pi_a p_{acc}\left(a \to b\right) A\left(a \to b\right) = \pi_b p_{acc}\left(b \to a\right) A\left(b \to a\right) \tag{2.14}$$

at this point we need to find expressions π_a, π_b, $A\left(a \to i\right)$ and $A\left(b \to a\right)$. First, let's analyze the energy situation of figure 3. Suppose there are n_1 links $+,+$ in the cluster boundary in a and n_2 links $-,-$ in b. These numbers indicate the number of neighbors tested and not included in the cluster, so the probability of a cluster such as a and b being formed is given, respectively, by:

$$\left(1-p\right)^{n_1} \tag{2.15}$$

$$\left(1-p\right)^{n_2} \tag{2.16}$$

which identifies our $A\left(a \to b\right)$ and $A\left(b \to a\right)$. The rationale for π_a and π_b is similar. We know that the probability of being in a certain state is given by its Boltzmann factor. To find it, we must obtain the energy in a and b, but the interactions within the cluster and in second (or more) neighbors have the same intensity in both states. Therefore, we only need to assess the energy balance through the contour of both clusters. The Boltzmann factor in a and b will be given, respectively, by:

$$\exp\left(-\beta(n_2 - n_1)\right) \tag{2.17}$$

$$\exp\left(-\beta(n_1 - n_2)\right) \tag{2.18}$$

Now we can rewrite equation 12 as:

$$\exp\left(-\beta(n_2 - n_1)\right)\left(1-p\right)^{n_1} p_{acc}\left(a \to b\right) = \exp\left(-\beta(n_1 - n_2)\right)\left(1-p\right)^{n_2} p_{acc}\left(b \to a\right) \tag{2.19}$$

Applying the metropolis acceptance criterion we then arrive at:

$$p_{acc}\left(a \to b\right) = min\left[1, \left(\frac{exp(-2\beta)}{1-p}\right)^{n_1}\left(\frac{1-p}{exp(-2\beta)}\right)^{n_2}\right] \tag{2.20}$$

Finally we can see why we add spins to the cluster with an arbitrary a priori probability, if we do from the beginning $p = 1 - exp(-2\beta)$ the cluster will be inverted with probability

1; there will be no rejection [3].

2.3 Comparisons

Both algorithms evolve the model in order to sample the distribution of states of the canonical ensemble and calculate the thermodynamic quantities correctly. At low temperatures, the overwhelming majority of single flip attempts are rejected, which can be understood through the Metropolis criterion or physically in terms of the coupling between the spins having a greater magnitude than the energy supplied by the reservoir. Thus, the system, prior to the critical region, is always close to the ground state. The cluster algorithm, in turn, at low temperatures, also does not leave the ground state, but emphasizes its degeneracy [1], since it forms clusters of approximately the size of the system and inverts them *always*, so the magnetization is almost always total, but with all spins either aligned downwards or upwards. Although this is expected, as the single flip gives very small steps in phase space, degeneracy does not arise naturally in its evolution. This is *fundamentally* related to ergodicity and Hamiltonian symmetry breaking which is the key feature of this phase transition. The *real* physical dynamics is *not* ergodic, therefore better described by the single spin flip algorithm.

In either high or low temperatures, despite the boost in dynamics at the phase transition, there is no fundamental efficiency gain [2]. After the critical region the clusters are formed by few spins (due to the low probability of inclusion), so there is also no great efficiency gain [2].

When motivating the development of another Monte Carlo dynamic, we mentioned low equilibration in the single spin picture when we are close to the critical region. Look at figure 6, referring to the Wolff dynamics which, close to a hypothetical critical temperature, starting from the ground state, balances the system 5 orders of magnitude faster than in figure 5, referring to the single flip dynamics. Both figures were made for an lattice of size 50. The equilibration time increases with size for both dynamics, but for the single spin flip algorithm the increase is greater than for the cluster one, a fact illustrated by figures 7 and 8.

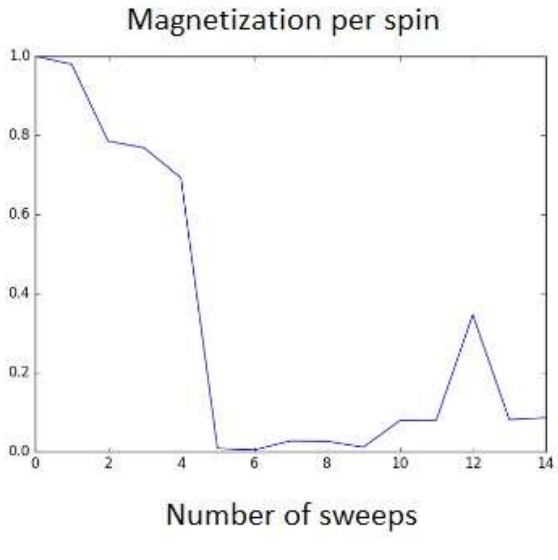

s

Figure 2.6: Equilibration for T=2.55 on edge 50. Note that the critical temperature is closer to the known analytical value.

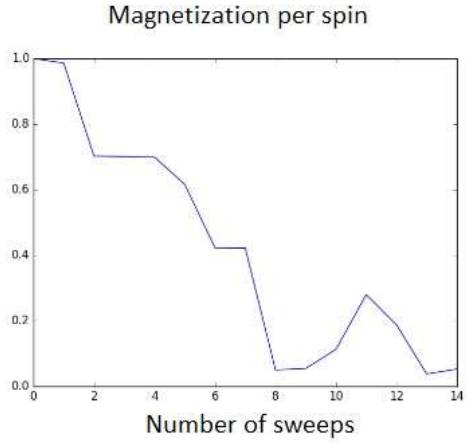

Figure 2.7: Wolff equilibrium at critical temperature for a 60x60 model.

2.4 Correlation Time and Dynamic Exponent

Formally, the difference in efficiency discussed in the previous section is related to the autocorrelation time of samples within the same temperature [2]. Remember that both dynamics follow Markov chains, that is, where we are in state space is directly dependent on where we were a step back. The autocorrelation time tells us the distance in steps between two points so that we can consider them uncorrelated [2]. As the single spin flip dynamics traverses the phase space slowly near criticality, for a long time we will be close to any given starting condition, while in the cluster dynamics the state space is traversed with greater speed, decorrelating samples in far less steps, a fact illustrated by Figures 9 and 10. .

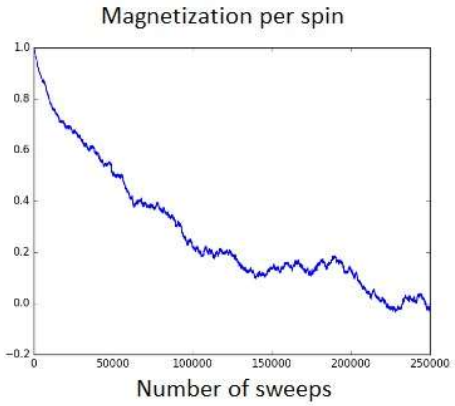

Figure 2.8: Single flip equilibration for a 60x60 model.

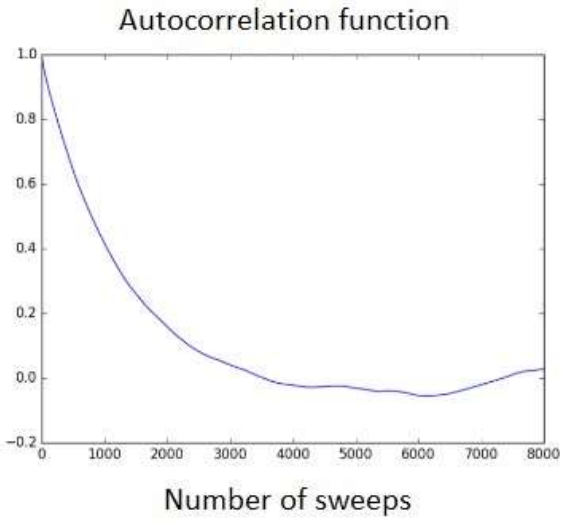

Figure 2.9: Autocorrelation function for a 16x16 system with single flip dynamics.

To study this behavior in more detail we need to define the dynamic exponent [2].

In the critical region we would like to express the autocorrelation time behavior as a power law [8]. We know in advance that the correlation length ξ (correlation between spins at different sites) diverges at the critical temperature. This information was implicit when we discussed the formation of clusters of the order of magnitude of the system in the region before the critical temperature. So, if we define the reduced temperature, which measures the deviation from the critical temperature, as:

$$t = \frac{T - T_c}{T_c} \tag{2.21}$$

we can write

$$\xi = |t|^{-\nu} \tag{2.22}$$

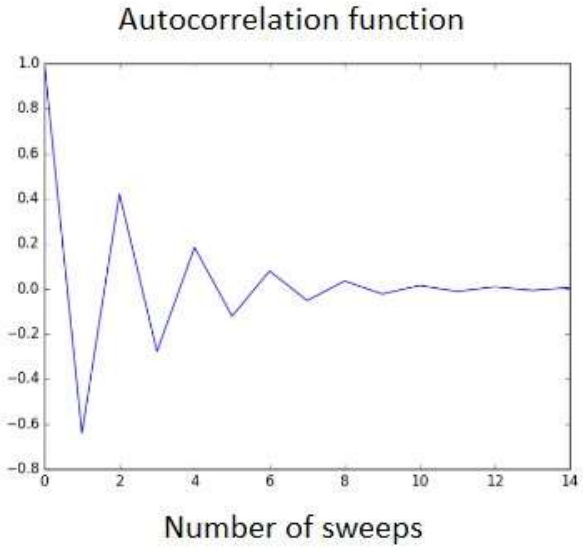

Figure 2.10: Autocorrelation function for a 16x16 system with Wolff dynamics.

where ν is a critical exponent to be evaluated later. We can now set the autocorrelation time as in [2]:

$$\tau = |t|^{-z\nu} \tag{2.23}$$

Where z is known as the dynamic exponent, the one that depends on the dynamics of the algorithm. Note that we can then write:

$$\tau = \xi^z \tag{2.24}$$

however, as our system is finite, the maximum correlation length is the edge of the system itself, hence:

$$\tau = L^z \tag{2.25}$$

Now we can quantitatively evaluate the difference in efficiency of the two dynamics. Just calculate the autocorrelation time for different sizes and linearize expression 25.

To calculate τ let's define the Time Shifted Autocorrelation Function [2]:

$$\chi(t) = \frac{1}{nm(0)^2} \sum_{i=0}^{n} m(i)m(t+i) \tag{2.26}$$

where $m(t)$ is the magnetization at time t (not to be confused with reduced temperature). The continuous function that best fits this function is an exponential of the type:

$$\chi(t) = exp\left(\frac{-t}{\tau}\right) \tag{2.27}$$

which, if we integrate:

$$\int_0^\infty \chi(t)dt = \int_0^\infty \exp\left(\frac{-t}{\tau}\right) dt = \tau \tag{2.28}$$

Then we kept the system at critical temperature, obtained approximately 10^7 samples for magnetization at each size and numerically integrated the expression 26. This procedure was performed for both algorithms and the corresponding linearized graphs are given by figure 11.

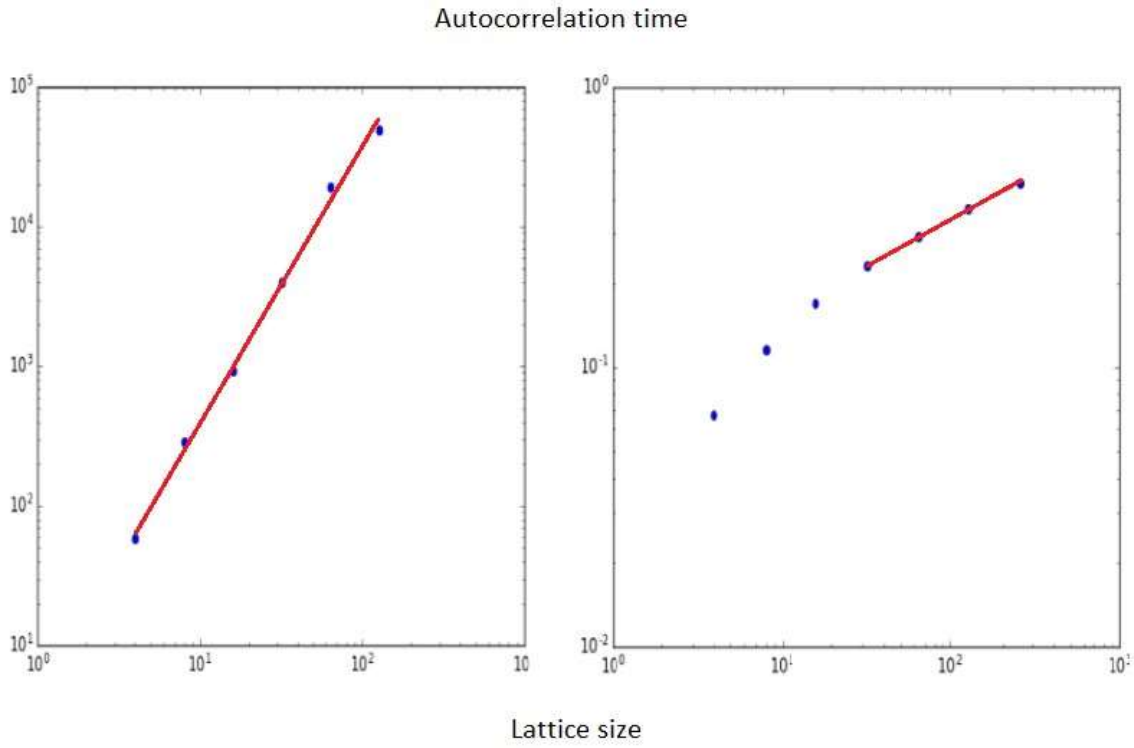

Figure 2.11: On the right, the linearization of the autocorrelation times from the cluster algorithm and on the left, from the single flip with $z = 1.92$ and $z = 0.32$, respectively.

The values found for the exponents are 1.92 and 0.32, respectively. The values differ from those found in the literature [2] (2.1665 and 0.25), however the objective here is to evaluate the difference in efficiency of the algorithms, and for this purpose these values are more than sufficient. They indicate how fast the correlation time grows near the critical temperature, and it is evident from the ratio between the exponents found that the single flip algorithm is slower than the cluster one.

2.5 Thermodynamic quantities and monte carlo measurements

In this subsection, the results for the Magnetization, Energy, Specific Heat and Magnetic Susceptibility will be presented, all by spin, and the comparisons with their respective analytical expressions.

The analytical expressions [8] used are, for magnetization:

$$m = (1 - \sinh(2\beta J)^{-4})^{1/8}, T < T_c \tag{2.29}$$

$$m = 0, T \geq T_c \tag{2.30}$$

for spin energy:

$$\epsilon(t) = -2J \tanh(2\beta J) + \frac{K}{2\pi} \frac{\mathrm{d}K}{\mathrm{d}\beta} \int_0^{\pi} \frac{\sin^2(\phi)}{\Delta(\Delta + 1)} d\phi \tag{2.31}$$

Where

$$K = \frac{2}{\cosh(2\beta J) \coth(2\beta J)} \tag{2.32}$$

and

$$\Delta = (1 - K^2 sin^2\phi)^{1/2} \tag{2.33}$$

for specific heat:

$$\frac{C(t)}{k} = \frac{2}{\pi} \left(\frac{2J}{kT_c}\right)^2 \left| -\ln\left(|1 - \frac{T}{T_c}|\right) + \ln\left(\frac{kT_c}{2J}\right) - \left(1 + \frac{\pi}{4}\right) \right|, T \approx T_c \tag{2.34}$$

First let's clarify how we calculate them from the Cluster Algorithm [2]. The energy of each sample is calculated by the definition of the Hamiltonian given by equation 1, the magnetization is given by the balance of aligned spins, the specific heat and susceptibility are proportional to the variance of energy and magnetization, respectively. After equilibration with the thermal reservoir, we can start to collect samples, since the energy of each one of them, for example, follows the distribution of states of the canonical ensemble. This indicates that the number of samples with energy E is proportional to the Boltzmann factor of E. So its expected value can be calculated directly from the arithmetic mean of the samples [2]. The same reasoning is valid for the other quantities. It is interesting to note that we are indirectly evaluating integrals and derivatives of the

uncalculated system partition function.

All the description given in the previous paragraph is also valid for the single flip algorithm [2], however the number of samples that we should obtain with this dynamic is much greater, because the energy difference between them is small, so so that if we consider the same amount for both dynamics, the spectrum of energies observed would be smaller for the single flip and the statistics acquired would not be so rich.

The first result to be discussed will be the spin magnetization. We can see from figure 12 that our statistical data (in blue) follows the analytical curve (red) with excellent

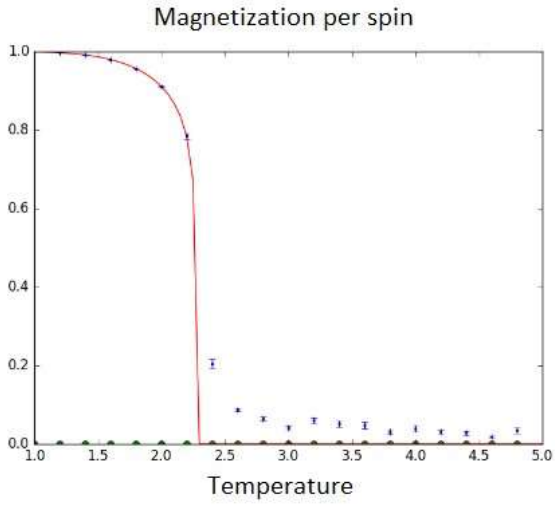

Figure 2.12: Spin magnetization on an edge system 50. Temperature is in $k_b T_c/J$ units

precision up to the critical temperature, beyond which the analytical expression is null. Nullity is not present predominantly due to two factors: we are not at the thermodynamic limit and we must use the absolute magnetization data, so the statistical fluctuations from the critical temperature that should change sign and on average vanish, are actually *sum* . The green dots at the bottom of the graph are the expected values of magnetization, which, due to dynamic encounter degeneracy, averages *zero* for all temperatures. The order disorder transition is successfully observed.

We now present the Magnetic Susceptibility in Figure 13. The analytical curve was obtained from the numerical differentiation of the magnetization. It is observed that the statistical data follows the analytical curve satisfactorily, since the system is finite, and there is a peak of the numerical data referring to the second-order phase transition.

The analytical specific heat, in turn, was also calculated via numerical energy differentiation, and is seen in figure 14. The statistical data are in good agreement with

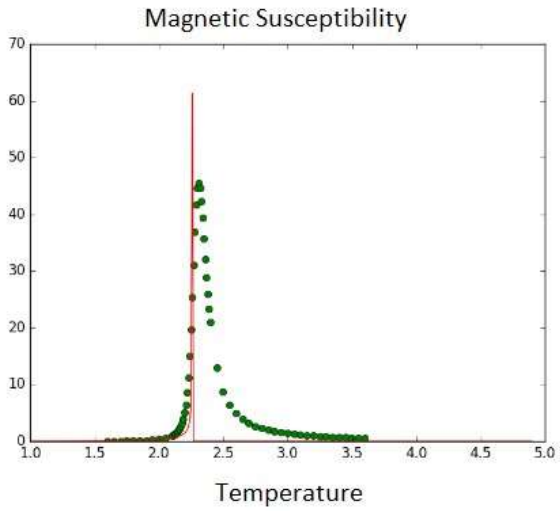

Figure 2.13: Spin magnetic susceptibility in a 50-edge system. Temperature is in $k_b T_c/J$ units

the analytical curve, also demonstrating a peak close to the critical temperature. It is worth mentioning that the divergence of the specific heat is logarithmic, therefore extremely slow. We must be extremely close to the critical temperature to see a peak of considerable size. The formal reason why the magnetic susceptibility peak is more salient will be given at the end of the next subsection.

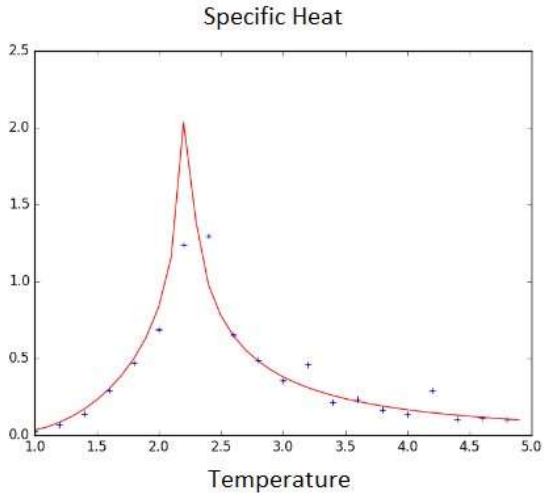

Figure 2.14: Spin specific heat in an edge system 50. Temperature is in $k_b T_c/J$ units

The energy per spin, finally, is perhaps the quantity that best corresponds to the analytical solution. Numerical data with error bar are completely contained in the red curve in figure 15.

Let us see the coherence between magnetization, energy and their derivatives.

While we are far from the critical temperature, their rates of change are low, if not null, a fact observed in figures 12 and 15. In the critical region, the growth and decrease of energy and magnetization, respectively, is *almost* vertical, indicating the peaks at 13 and 14.

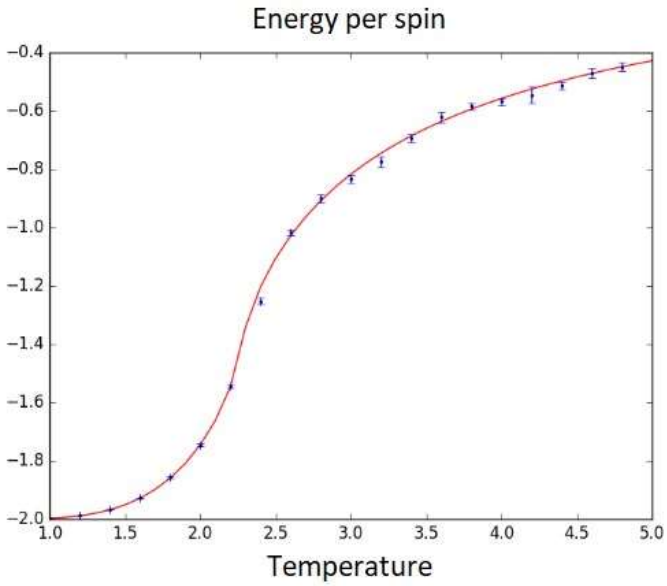

Figure 2.15: Energy per spin in a 50× 50 lattice.

2.6 Interlude : Spin blocks, scaling and universality

In the introduction I tryed to convey how importante the Ising model is in the development of statistical mechanics as a whole. This section deepens this idea by presenting the seeds of the so called Renormalization Group Theory. The Ising model, from a statistical mechanical point of view at least, was the main motivation for the development of such ideas and techniques, and in doing so it establishes a deep connection from condensed matter and quantum field theory. Unfortunatelly the complete development of these concepts is out of the scope of this thesis. Still, to provide a thorough presentation of the 2D ferromagnetic phase transition it is mandatory to compute critical exponents, therefore we will explore a little this topic.

I will lay out the main ideas of the renormalization transformations and with them discuss fixed points of the renormalization flow. We will get to the concept of universality and derive the power law behavior at the critical region, also deriving the scaling relations

between critical exponents.

2.6.1 Renormalization Group Flow

We start by noticing a curious fact: self similarity. Self similarity, by definition, means scale invariance: Zooming in or out makes no difference, the system is the same at all scales. Scale invariance is at the heart of the renormalization process and has universality as a consequence[11]. Here we merely take self similarity for granted.

We consider a more complex hamiltonian in this case, accounting for next-nearest-neighbor interactions as well, a choice which will be justified later.

$$-\beta H_s = J \sum_{nn} s_i s_j + K \sum_{nnn} s_i s_j \tag{2.35}$$

We will now define a course graining procedure which will lead blocks of four spins to behave as one single spin, scaling the lattice, in a way such that the partition function of the original system is unchanged. Figure 2.16 illustrates the procedure.

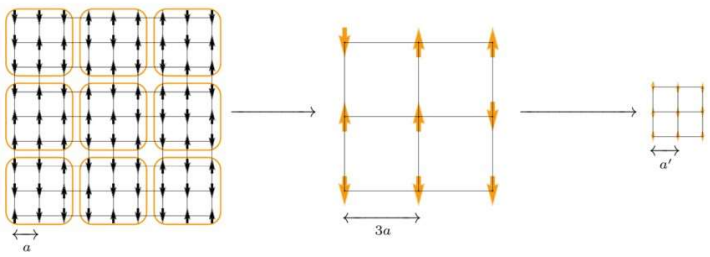

Figure 2.16: Renormalization procedure. Adapted from [12]

We choose the orientation following some simple rules: divide the lattice in blocks of four spins so that the orientation of the equivalent new spin t_k will be up if more than 2 spins are up, down if more than 2 are down and up or down with equal probabilities otherwise.

$$\begin{aligned} t^k(s_1^k, s_2^k, s_3^k, s_4^k) &= 1, \sum s^k > 0, \\ t^k(s_1^k, s_2^k, s_3^k, s_4^k) &= -1, \sum s^k < 0, \\ t^k(s_1^k, s_2^k, s_3^k, s_4^k) &= \pm 1, \sum s^k = 0, \end{aligned} \tag{2.36}$$

s

Therefore it is possible to define a probability density

$$\begin{aligned} W = 1, \quad & \sum_i s_i^k > 0, t^k = 1 \\ W = 1, \quad & \sum_i s_i^k < 0, t^k = -1 \\ W = 0.5, \quad & \sum_i s_i^k = 0, t^k = 1 \\ W = 0.5, \quad & \sum_i s_i^k = 0, t^k = -1 \\ \Rightarrow \sum_{t^k} & W\left(t^k, s_1^k, s_2^k, s_3^k, s_4^k\right) = 1 \quad \text{for any set of } s_i^k \end{aligned} \tag{2.37}$$

And a new (truncated) Hamiltonian, which governs the behaviour of the t^k

$$-\beta H_{t^k} = J' \sum_{nn} t_i^k t_j^k + K' \sum_{nnn} t_i^k t_j^k \tag{2.38}$$

Such that the new boltzmann factor is

$$e^{-\beta H_{t^k}} = \sum_{s_i^k = \pm 1} e^{-\beta H_{s_i}} W\left(t^k; s_1^{(k)} \dots s_4^{(k)}\right) \tag{2.39}$$

and the new partition function becomes

$$Z' = \sum_{t^k} e^{-\beta H_{t^k}} = \sum_{t^k} \sum_{s_i^k = \pm 1} e^{-\beta H_{s_i}} W\left(t^{(k)}, s_1^{(k)} \dots s_4^{(k)}\right) \tag{2.40}$$

and finally commuting the sum

$$Z' = \sum_{s_i^k = \pm 1} e^{-\beta H_{s_i}} \sum_{t^k} W\left(t^{(k)}, s_1^{(k)} \dots s_4^{(k)}\right) = Z, \text{ for } \sum_{t^k} W = 1 \tag{2.41}$$

So, transforming from fine to coarse spins and truncating the hamiltonian leaves the thermodynamic properties unchanged.

This procedure is called renormalization. It scales distances up and defines a mapping of (J, K) onto (J', K'). If we proceed iteratively this defines a flow in the $J \times K$ space. First, let us understand how it should look.

At $T < T_C$ most spins align, so the coarse graining tends to worsen the disparity between the up and down directions. As the excitations from the ground state die out,

the block spins t^k will generate a greater magnetization. Here, our flow takes us to lower temperature states with an attractor at the ground state.

At $T > T_c$, the renormalization procedures further increases the randomness of the spin blocks, decreasing correlations. Therefore the flow takes us to higher temperatures with an attractor at infinity.

At the critical region we could argue that by continuity of the flow there should be a saddle point. Let us instead argue that by the very definition of scale invariance the coarse graining procedure will return the system to its own initial state. The last three paragraphs build fig 2.17

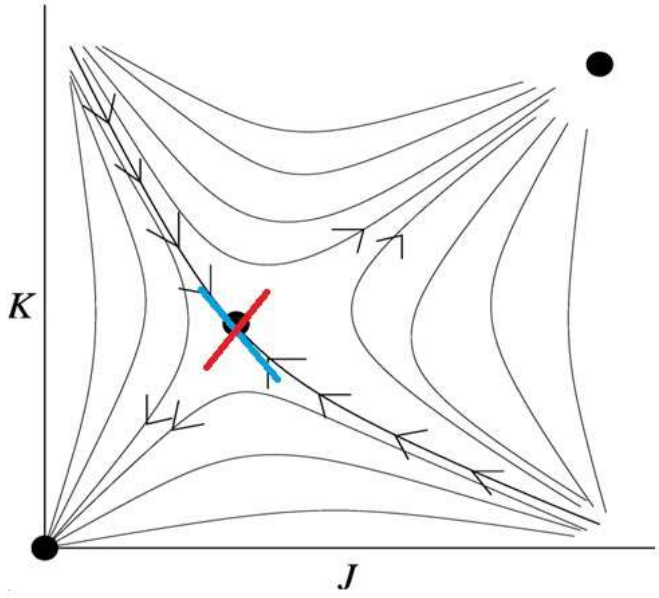

Figure 2.17: Renormalization group flow in parameter space. The blue and red lines represent eigenvalues of the **A** operator. Adapted from [13]

Now we are all set to define critical exponents and their relations.

Eigenvalues and Scaling

The power law behavior of physical quantities at the phase transition stems from a linear expansion at the saddle point of fig 2.17, so we start by defining small perturbations from the (J^*, K^*) saddle point.

$$\begin{aligned} J' &= J^* + \Delta J, \\ K' &= K^* + \Delta K \end{aligned} \tag{2.42}$$

such that in the next iteration

$$(J^* + \Delta J, K^* + \Delta K) \overset{\text{rescaling}}{\longrightarrow} (J^* + \Delta J', K^* + \Delta K') \tag{2.43}$$

we are still in the linear approximation. We can write this process as a linear operator $\mathbf{A}$ acting on the (J, K) space:

$$\begin{pmatrix} \Delta J' \\ \Delta K' \end{pmatrix} = \mathbf{A} \begin{pmatrix} \Delta J \\ \Delta K \end{pmatrix} \tag{2.44}$$

Now, inspecting fig 2.17 we realize $\mathbf{A}$'s eigenvectors and eigenvalues are built in the flow. Applying $\mathbf{A}$ to the points in the blue and red lines take them on to the same direction, therefore those are the eigenvectors of $\mathbf{A}$. Furthermore, if we call λ and μ its eigenvalues, we know from the convergence/divergence of flow that $\lambda < 1$ and $\mu > 1$.

Now, remember that applying $\mathbf{A}$ rescales the system. In the example given here the scaling is by a factor of 2, but had we chosen another size for our initial block then this factor could be arbitrary. We will call it l. This is to say that applying $\mathbf{A}$ n times would yield λ^n and μ^n eigenvalues while the rescaling would yield a factor of l^n. We conclude:

$$\begin{aligned} \lambda\left(l^n\right) &= \lambda^n(l) \\ \mu\left(l^n\right) &= \mu^n(l) \\ \Rightarrow \lambda = l^y, \quad \mu &= l^z. \end{aligned} \tag{2.45}$$

Now we are able to choose a random vector $\vec{v}$ in the vicinity of the saddle point and observe its behavior under the flow.

$$\vec{v} = t\hat{t} + s\hat{s}, \quad \text{so} \quad (J, k) \leftrightarrow (t, s) \tag{2.46}$$

where

$$\begin{aligned} \mathbf{A}\hat{s} &= \lambda\hat{s} \\ \mathbf{A}\hat{t} &= \mu\hat{t} \\ \mathbf{A}^n(s\hat{s} + t\hat{t}) &= sl^{yn}\hat{s} + tl^{zn}\hat{t} \end{aligned} \tag{2.47}$$

Now we introduce the correlation length of spin orientation, which is zero at high temperatures and the size of the lattice at low temperatures. At the thermodynamic limit, approaching T_c from above, this length diverges but want to understand *how*, namely

what is its asymptotic behavior.

$$\begin{aligned} &\xi\left(T < T_c\right) \to L \\ &\xi\left(T > T_c\right) \to 0 \\ &\xi\left(T \sim T_c\right) \to ? \end{aligned} \tag{2.48}$$

To answer this question we note that with each renormalization process ξ is rescaled:

$$\xi\left(s', t'\right) = \xi(s,t)/l \tag{2.49}$$

after n rescalings:

$$\xi\left(l^{ny}s, l^{nz}t\right) = \xi(s,t)/l^n \tag{2.50}$$

and since t is small, there is n such that

$$\begin{aligned} &l^{nz}t = 1 \\ &\to l^n = t^{-1/z} \end{aligned} \tag{2.51}$$

such that

$$\begin{aligned} \xi\left(t^{-y/z}s, 1\right) &= \xi(s,t)t^{1/z} \\ \to \xi(s,t) &= t^{-1/z}\xi(0,1) \end{aligned} \tag{2.52}$$

interpreting $t = |T - T_c|$. Therefore

$$\xi \sim |T - T_c|^{-1/z} = |T - T_c|^{-\nu} \tag{2.53}$$

We conclude that the power law behavior of the correlation length can be derived from the intrinsic scale invariance of the system.

Next in line are other measurable physical quantities. To analyze them we need to turn our attention to the free energy. Since the partition function is invariant under our transformations, so will be the free energy. Now, during spin-blocking the number of spins decreases so we must account for this in the free energy per spin,

$$f\left(s', t'\right) = \frac{F\left(s', t'\right)}{N/l^d} = l^d \frac{F(s,t)}{N} = l^d f\left(s,t\right) \tag{2.54}$$

To analyze the magnetic susceptibility we need to extend the hamiltonian, adding

a small magnetic field and later taking it equal zero

$$-\beta H = J\sum s_i s_j + K\sum s_i s_j + h\sum s_i \tag{2.55}$$

Such that the matrix $\mathbf{A}$ is 3×3 with 3 eigenvalues λ, μ, k. Since h breaks symmetry by existing, it destroys the critical behavior and will not return the system to the saddle point, so we conclude $k > 1$. Performing the same previous analysis we get to the conclusion that

$$\rightarrow f\left(l^{ny}s, l^{nz}t, l^{nv}h\right) = l^{nd}f(s,t,h) \tag{2.56}$$

Now, taking $h = 0$, t small and n large such that $l^{nz}t = 1$ we get $l^{ny}s \rightarrow 0$ with s small and because $y < 0$. Therefore

$$f(s,t,0) = l^{-nd}f(0,1,0) = t^{d/z}f(0,1,0) \tag{2.57}$$

Now, moving on to the specific heat

$$\begin{aligned} c_h &= T\frac{\partial^2 f}{\partial T^2} \\ c_h &\sim t^{d/z-2} = t^{-\alpha}, \text{ by deffinition} \end{aligned} \tag{2.58}$$

and, since $\nu = 1/z$,

$$\alpha = 2 - d\nu \tag{2.59}$$

and now for the magnetization

$$\begin{aligned} m &= \frac{\partial f}{\partial h} = t^{d/z-v/z}\frac{\partial f}{\partial h}\left(0,1,t^{-v/z}h\right) \\ m &\sim t^{-\beta}, h = 0 \\ \beta &= (d-v)\nu \end{aligned} \tag{2.60}$$

and for the susceptibility

$$\begin{aligned} \chi = \left[\frac{\partial m}{\partial h}\right]_{h=0} &= t^{d/z-2v/z}\frac{\partial^2 f}{\partial h^2}(0,1,0) \quad \sim t^{-\gamma} \\ \rightarrow -\gamma &= (d-2v)\nu \end{aligned} \tag{2.61}$$

The previous three equations are called scaling relations. We combine them to eliminate

v and d:

$$\rightarrow \alpha + 2\beta + \gamma = 2 \tag{2.62}$$

Now we go back to eq. 2.56. We are not going to assume zero h, instead we study the system at exactly T_c and analyze the behavior of the magnetization as $h \rightarrow 0$. Choose v samall and n large such that $l^{nv}h = 1$:

$$f(s, 0, h) = h^{d/v} f(0, 0, 1) \tag{2.63}$$

Then

$$m = \frac{\partial f}{\partial h} \sim h^{d/v-1} \rightarrow \frac{1}{\delta} = \frac{d}{v} - 1 \tag{2.64}$$

and combining with the scaling relations for β and γ

$$\rightarrow \beta(\delta - 1) = \gamma \tag{2.65}$$

Now, the derivation of the power law behavior for the correlation function, despite being very similar in spirit, is much more envolved and can be found in pages $234-235$ of ref [4]. We will mention the result:

$$g(r) \sim \frac{1}{r^{d-2+\eta}} \tag{2.66}$$

And note that

$$\frac{\partial m}{\partial h} \propto \sum_k \left(\langle s_k s_j \rangle - \langle s_k \rangle \langle s_j \rangle \right) = \sum_k g(k, j) \tag{2.67}$$

Such that in the continuum limit

$$\begin{aligned} \frac{\partial m}{\partial h} &\sim \int g(r) d^d r \\ \frac{\partial m}{\partial h} &\sim \int_0^{\xi} \frac{1}{r^{d-2+\eta}} r^{d-1} dr = \xi^{2-\eta} = t^{-\nu(2-\eta)} \end{aligned} \tag{2.68}$$

And combining with eq. 2.60, we have

$$\gamma = \nu(2 - \eta) \tag{2.69}$$

In summary, all the scaling relations are

$$\begin{aligned} \alpha + 2\beta + \gamma &= 2 \\ d\nu &= 2 - \alpha \\ \beta(\delta - 1) &= \gamma \\ \gamma &= \nu(2 - \eta) \end{aligned} \tag{2.70}$$

It is important to notice that there are only two independent variables in this system of equations, thus computing any two of them will yield all others.

2.6.2 Universality

The origins of universality could have been discussed straight from the RG flow section. Instead I chose to first derive *what* is universal, the critical exponents.

First in this discussion I want you to notice that our discussion in the last two sections is not different in the slightest if our hamiltonian had been defined in a triangular or honeycomb lattice. Thus the critical behavior is the same in those lattices: Our first unbelievably beautiful result.

Second, no matter what the initial values for K and J are, due to the RG flow in the saddle point, every system will behave the same. That is to say, systems with only nearest neighbor or only next nearest neighbor interactions will have the same behavior near criticality. This can be extended to any number of ferromagnetic next neighbor interactions with the same symmetry. This is our second unbelievable result.

Third and last, to understand how gases, for instance, are in the universality class of the Ising model, in the lattice gas aproximation, their hamiltonians are the same as the Ising model's. Since the many other interactions not considered are irrelevant under RG flow, indeed they should belong to the same universality class.

We will now end this chapter in the next section performing finite size scalling on our monte carlo data to compute all the critical exponents in the Ising universality class.

2.7 Critical Exponents and Finite Size Scaling

In order to complete the characterization of the phase transition we must find the critical exponents of the analytical solution [8]. As derived in the previous section, we will describe the behavior of magnetic susceptibility in the vicinity of the critical temperature as a power law. We know that:

$$\chi = |t|^{-\gamma} \tag{2.71}$$

$$\xi = |t|^{-\nu} \tag{2.72}$$

The key idea behind finite size scalling is to interpret equilibrium samples of different sizes as steps in the RG transformations. This is to say, samples of different sizes at the vicinity of the critical temperature are block spins of each other.

As mentioned in the last section, only two exponents are required to determine all of them, so we focus on γ and ν.

We define the so called susceptibility scaling function:

$$\bar{\chi} = \chi L^{-\frac{\gamma}{\nu}} \tag{2.73}$$

Since $\chi \sim \xi^{\gamma/\nu}$ and $\xi \sim L$ in finite systems, plotting this quantity for different sizes as a function of the reduced temperature will yield the same result provided that the critical exponents γ, ν and T_c are found correctly. This is a very simplified version of the full finite size scalling scheme, but it is correct and yields the right results in this case. A full account can be found in [5]. We then tried with different values for γ, ν and T_c and identified the combination that generates the overlapping curves.

The following figures, except for 16, refer to the data treatment developed here. In figure 16, we plot the magnetic susceptibility values without any treatment. It is observed that the peak increases with size and the temperature at which this occurs shifts to the left. The value found for the critical temperature at an edge 200 was 2.28.

Figure 17 refers to $\bar{\chi}(T)$, the susceptibility scaling function, setting every exponent to one. It is remarkable that it already brings the susceptibility of all sizes to the same order of magnitude, demonstrating its effectiveness; the peak for edge 200 was 3 orders of magnitude greater than for edge 10. Figure 18 was made in search of the critical exponents, with γ=2, ν=1.1 and $T_c = 2.28$. Figure 19, finally, shows the curves fully

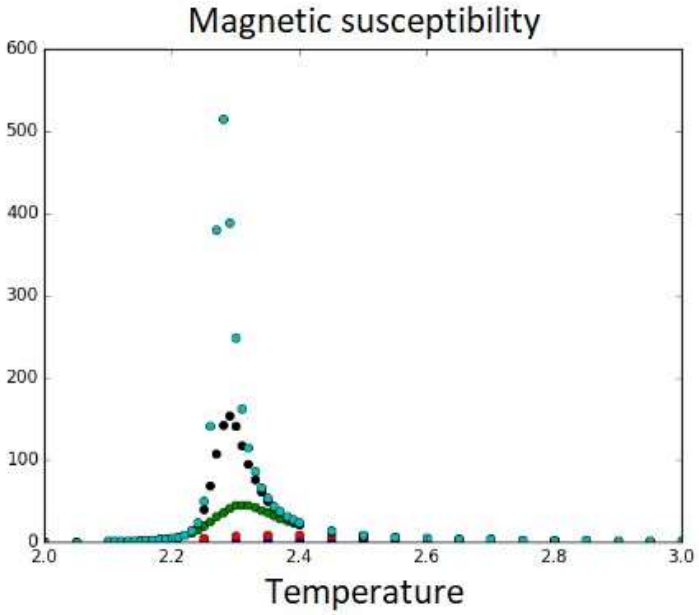

Figure 2.18: Spin magnetic susceptibility in systems of size 10, 20, 50, 100 and 200, in ascending order of peaks.

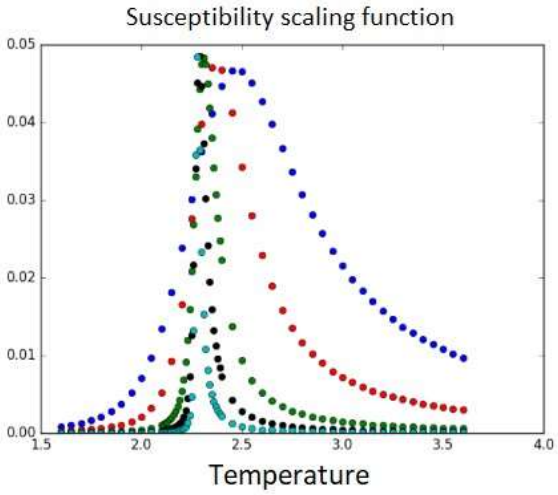

Figure 2.19: susceptibility scaling function on 10, 20, 50, 100 and 200 size systems, in descending order of width.

overlapping with the critical exponents and temperature identified as:

$$\begin{aligned} \gamma &= 1.75 \\ \nu &= 1 \\ T_c &= 2.269 \end{aligned} \tag{2.74}$$

With these results in hand we can backsubstitute in eq 2.70 to find all of the critical

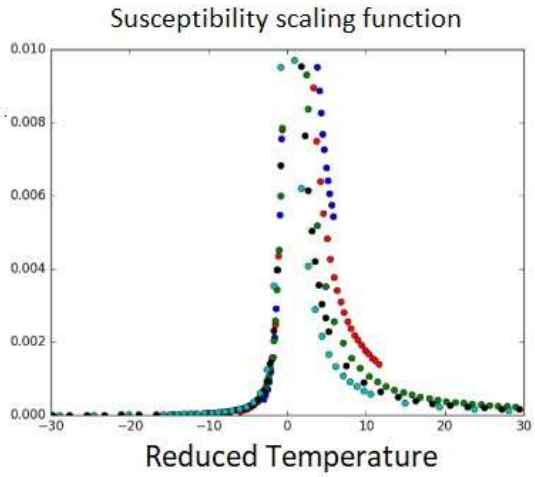

Figure 2.20: susceptibility scaling function for sizes 10, 20, 50, 100 and 200. The parameters used were $\gamma = 2$, $\nu = 1.1$ and $T_c = 2.28$.

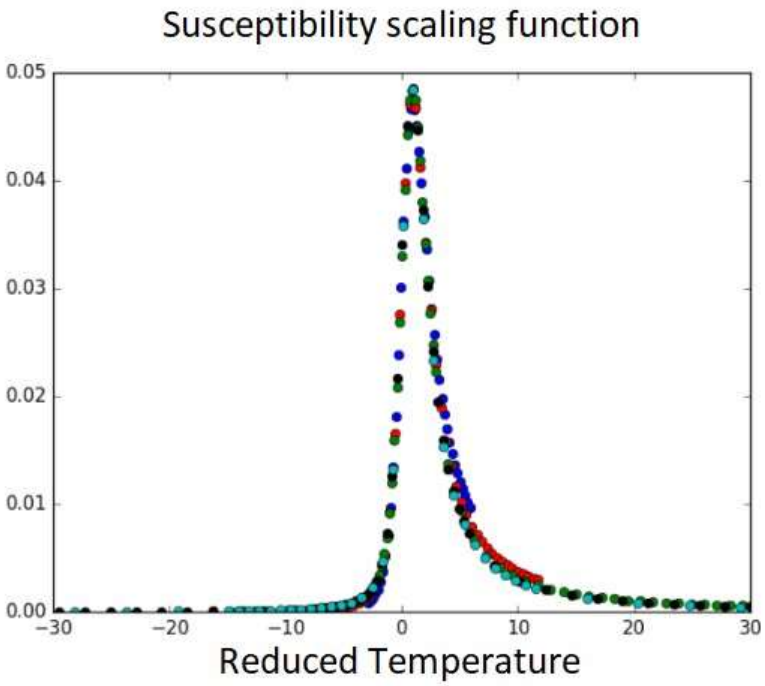

Figure 2.21: Superimposed susceptibility curves that identify $T_c = 2.269$, $\gamma = 1.75$ and $\nu = 1$.

exponents of the phase transition. We find:

$$\begin{aligned} \alpha &= 0 \\ \beta &= 1/8 \\ \delta &= 15 \\ \eta &= 1/4 \end{aligned} \tag{2.75}$$

We now consider to have done a solid and thorough exploration of the phase transition and may now move on to more complex models.

Chapter 3

Frustrated Ising Models

This chapter relies heavily on refs [14] and [15]

3.1 Frustration as a relevant phenomenom

Frustration in spin systems is subject of intense research, both theoretical and experimental. The first such system is the triangular lattice 2d antiferromagnetic Ising Model. The low temperature state will try to satisfy as many bonds as possible, but since it is impossible for three spins on a single unit cell to be antiparallel, great degeneracy arises and no long range order is present even at zero temperature. Therefore no phase transition occurs. The quest for understanding the very interesting behaviors these systems exibit has lead to the discovery of spin liquids, spin ice, and in turn these phenomena have been linked to many interesting phenomena. In the past few decades, for instance, frustration has been linked to superconductivity. One of the interests of my masters project was to enter the field, introducing such concepts, learning to simulate and analyze these systems. In this section I briefly summarize the theoretical results obtained via transfer matrix computations for the models subject to scrutiny in[16].

3.2 The transfer matrix

Before presenting the model and results, it is necessary to introduce the transfer matrix technique, which is of crucial importance in the analytical study of spin systems.

We start by considering the 1D ferromagnetic Ising chain with periodic boundary conditions. Its Hamiltonian can be written as

$$H = -J\sum_n S_n S_{n+1} - h\sum_n S_n \tag{3.1}$$

so the partition function

$$Z_N(H,K) = \ Tr\left(exp\left(K\sum_n S_n S_{n+1} + H\sum_n S_n\right)\right) \tag{3.2}$$

with

$$K = -\frac{J}{k_b T}, \quad H = -\frac{h}{k_b T} \tag{3.3}$$

can be rewritten as

$$Z_N = \sum_{S_1=\pm 1} ... \sum_{S_N=\pm 1} \prod_{n=1}^{N} \exp\left(K S_n S_{n+1} + \frac{H}{2}(S_n + S_{n+1})\right), \tag{3.4}$$

provided that $S_{N+1} = S_1$. Now we introduce the transfer matrix $\mathbf{T}$ whose elements are defined by

$$\mathbf{T}_{S_n,S_{n+1}} = \exp\left(K S_n S_{n+1} + \frac{H}{2}(S_n + S_{n+1})\right) \tag{3.5}$$

so that

$$\mathbf{T} = \begin{bmatrix} T_{1,1} & T_{1,-1} \\ T_{-1,1} & T_{-1,-1} \end{bmatrix} = \begin{bmatrix} e^{H+K} & e^{-K} \\ e^{-K} & e^{-H+K} \end{bmatrix} \tag{3.6}$$

The trick is to realize that the partition function in terms of the matrix elements

$$Z_N = \sum_{S_1=\pm 1} ... \sum_{S_N=\pm 1} \prod_{n=1}^{N} \mathbf{T}_{S_n,S_{n+1}}, \tag{3.7}$$

is actually the trace of the matrix $\mathbf{T}^N$

$$Z_N = Tr\left(\mathbf{T}^N\right) \tag{3.8}$$

Now, since $\mathbf{T}$ is symmetric, we can write it in diagonal form and realize that its trace is merely the sum of its eigenvalues,

$$Z_N = \lambda_+^N + \lambda_-^N, \quad \lambda_+ > \lambda_- \tag{3.9}$$

then, in the thermodynamic limit, the asymptotic behaviour becomes

$$\lim_{N\to\infty} Z_N = \lim_{N\to\infty} \lambda_+^N \left(1 + \left(\frac{\lambda_-}{\lambda_+}\right)^N\right) \sim \lambda_+^N \tag{3.10}$$

and the free energy per spin becomes

$$f = -K_b T \ln(\lambda_+) \tag{3.11}$$

Now, diagonalizing $\mathbf{T}$, its eigenvalues are

$$\lambda_\pm = e^K \left(\cosh(H) \pm \sqrt{\sinh^2(H) + e^{-4K}}\right) \tag{3.12}$$

such that the free energy is

$$f = -J - k_b T \ln\left(\cosh(H) + \sqrt{\sinh^2(H) + e^{-4K}}\right) \tag{3.13}$$

which is the expression found by Ising in 1925 and lead him to abandon physics. This derivation will be useful to analyze the ground state of the PUD model.

3.3 PUD model

The Pilled-up Dominoes model can be described by a square lattice Ising Model with periodically alternating interactions J and J' columnwise as in fig 3.1. Its Hamiltonian is of the same functional form as previously shown, but now the coupling constant changes periodically. We are free to vary these parameters and will actually present results for the variation $\tilde{J}$ of their ratio.

The system features three stable phases, antiferromagnetic, paramagnetic and ferromagnetic. These are critical lines, not coexistence ones. It also features a zero temperature phase transition to a spin glass at $\tilde{J} = -1$.

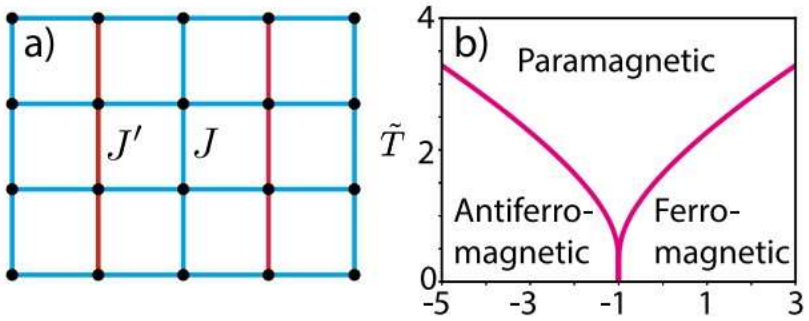

Figure 3.1: PUD model definition and phase diagram. These are not coexistence lines, every transition in this phase diagram is critical.

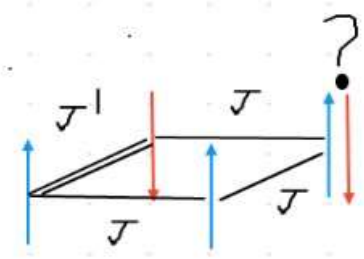

Figure 3.2: Frustrated Plaquette

The first fact to be explicitly shown is that this system is frustrated. Observe in fig 3.2 that never all bonds can be satisfied. It is in contrast with the antiferromagnetic triangular Ising Model, for here frustration arises not from the lattice topology, rather it does from competing interactions, not present in the former.

Let us qualitatively analyze the groundstate when $\tilde{J} << -1$ or $T \to 0$ and $\tilde{J} < -1$. It is clearly energetically favourable in this region to satisfy the antiferromagnetic bonds, vertically alternating up and down spins. Therefore the ground state has two options for the odd antiferromagnetic columns: either they are in or out of phase. If out of phase, the spins in the middle necessarily have one frustrated bond either to the left or to the right so that the maximum number of satisfied bonds equal three. If they themselves don't satisfy their ferromagnetic bonds with their even fellows vertically, energy increases even more, indicating that the only two possible states for even (ferromagnetic) columns in a ground state of out of phase odd strings are either all up or all down, so only two.

On the other hand, if both odd strings are in phase, the maximum amount of stisfied bonds is now 4 (which won't happen very often), plus now there are much more than two possibilities for laying out spins in the even ferromagnetic columns.

We conclude that this increase in entropy of the in phase ground state favours it

over the out of phase configuration. Indeed, this situation gives rise to a macroscopic degeneracy in the ground state, which is derived formally in the next session. This is also strongly hinted in my paper by machine learning techniques.

3.4 Exact antiferromagnetic ground state computations

The conclusion that the ground state is composed of in phase antiferromagnetic strings greatly simplifies calculations for zero temperature. We now only have to consider the dynamics of the even ferromagnetic strings in a staggered magnetic field, producing a reduced hamiltonian of the form

$$H_{red} = -J\sum_n S_n S_{n+1} - 2J\sum_n (-1)^n S_n \tag{3.14}$$

which allows us to use a very similar procedure to that derived for the standard 1D Ising chain. The main difference is that now due to the sign change of odd rows, the transfer matrix becomes the following product of two matrices

$$T = \begin{bmatrix} e^K & e^{-K-H} \\ e^{-K+H} & e^K \end{bmatrix} \begin{bmatrix} e^K & e^{-K+H} \\ e^{-K-H} & e^K \end{bmatrix} \tag{3.15}$$

the first representing a transition from a $2n-1$ to a $2n$ site and the second from the $2n$ to a $2n+1$ site. This caveat turns the partition function into the square root of the largest eigenvalue

$$Z = \sqrt{e^{2K} + e^{-2k}\cosh 2H + \sqrt{e^{4K} + e^{-4K}\cosh^2 2H + 2\cosh 2H + 2(1-\cosh 4K)}} \tag{3.16}$$

such that taking the derivative with respect to H and plugging in $H = 2K$, the staggered magnetization is

$$m_{stag} = \frac{\sqrt{2}\sinh(2K)}{\sqrt{2\exp(4K) + \cosh(4K) - 1}} \tag{3.17}$$

and now taking the zero temperature limit

$$\lim_{K\to\infty} m_{stag} = \frac{1}{\sqrt{5}} \tag{3.18}$$

Performing the same steps for the entropy yields

$$S = \frac{1}{4} \ln \left(\frac{3+\sqrt{5}}{2} \right) \tag{3.19}$$

Both results are in agreement with [15]. Furthermore, these are the exact values for the ground state when the global system is considered in the transfer matrix approach.

It is interesting to notice the macroscopic degeneracy arising in this model. The ground state is ordered, as evidenced by the staggered magnetization, so despite macroscopic entropy being present the ground state presents correlation. That is to say, this is not trivial behavior.

3.5 ZZD model

The next frustrated Ising system I studied is the ZZD model. It is also aranged in a square lattice with periodic frustration. The main difference from the PUD model is the columnwise alternation dependence on the row. In each fixed row the J' interaction alternates out of phase with respect to adjacent rows. The situation is depicted in fig. 3.3

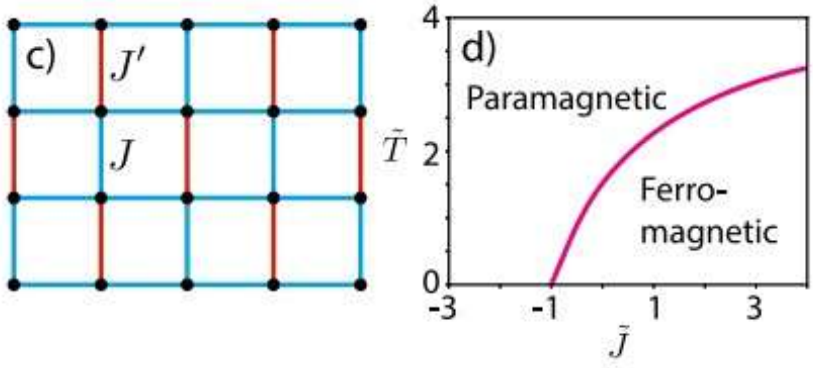

Figure 3.3: The Zig-Zag Dominoes model and its phase diagram.

Despite the clearly simpler phase diagram, contrasting with the PUD model, there is no ground state assumptions we could make to present a simple but effective transfer matrix computation in any regime. In fact, this slight asymmetry regarding the J' bonds makes computations extremely more difficult, to a point that ordering at $T = 0$ remained an open question for a very long time.

We will mention interesting facts without proof, by mere handwave arguments. First, at $T = 0, \quad \tilde{J} = -1$, both (PUD and ZZD) models are the same through a Mattis transform and are the same as a fully random J, J' arrangement, a spin glass.

Second, in different limits it behaves as different Ising models, such that solving this problem is solving various models. Qualitatively, we argue that in the $\tilde{J} \to -\infty$ regime, since every J' bond will be satisfied, if we assign "up" for a (up, down) and "down" to a (down, up) pair, in the thermodynamic limit, we end up in the ground state of a triangular antiferromagnetic lattice.

Similarly, in the $\tilde{J} \to \infty$ limit the model behaves as a triangular ferromagnetic Ising model. In the $J' = 0$ regime, this model is exactly the same as an hexagonal ferromagnetic lattice, and, obviously, at $J' = J$ it is the standadard square lattice ferromagnetic Ising model.

All of these facts can be shown analytically. Despite these intere sting exact computations, nothing is said about the critical exponents, from either model, in the $J' < J$ region.

We conclude the presentation of these models emphasizing how non-trivial their behavior is and how difficult it is to get to any result, either analytically or computationally. For instance, the high degeneracy of the PUD antiferromagnetic ground state obliges very slow cooling to achieve in a monte carlo procedure. Having achieved it, it is an even more difficult task to acquire uncorrelated samples for meaningful averages. Frustration represents a great challenge to physicists, and any progress in accurate conclusions with small datasets and simple techniques is of great help. This is the result of our paper.

Now, all this challenge is only worth it if there are experimental realizations of such systems. In the next chapter I give examples of experimental results which motivate the task force in solving frustrated spin problems.

Chapter 4

Experimental realizations of Ising Models

This chapter relies heavily on the survey "The Ising Model and Real Magnetic Materials" by W. P. Wolf [17]. It discusses in depth the interplay of theory, simulation and experiments of various materials. Every picture, table and discussion present in this chapter can be found there.

4.1 Standard Ising models

The goal of this chapter is not to explain deeply in detail why or how materials come to behave as Ising Models. Rather, the intention is to state some facts and display the power of theory against some actual measurements in actual materials, therefore justifying the amount of effort put in developing the theory of phase transitions and efficient Monte Carlo algorithms.

The arguments regarding why some compounds are Ising-like are very involved. We need to study the behavior of magnetic ions in a crystalline environment, which is not an easy task. Generally speaking, though, two criteria must be met for such a situation to arise. First the ground state of the ion must be a doublet well separated from excited states, so that the strictly up or down spins are faithfully represented, second these states cannot be coupled. The coupling constant between neighbors is free to assume different values from site to site and a number of nearest neighbors can be accounted for such that the hamiltonian is still Ising-like. The table below brings some examples of materials with these features.

Chemical Formula	Magnetic Structure	Ordering	$T_c(K)$	$\Delta E/k_B T_c$
$Dy^2(C_2H_5SO_4)_3.9H_2O$	Coupled chain	Dipolar ferromagnet	01	~ 190
$Dy^2C_3Al_5SO_{12}$(DyAlG)	Cubic garnet	6-sublat.antiferro.	25	27
$DyPO_4$	Cubic diamond	2-sublat.antiferro.	34	20
$LiTbF_4, LiHoF_4$	b.ct.trigonal	Dipolar ferromagnet	29	> 50
Rb_2CoF_4, K_2CoF_4	Coupled planes	2d antiferromagnet	101	~ 4
$Dy_2Ti_2O_7$	Cubic pyrochlore	Frustrated "spin ice"	< 0.05	> 100

Figure 4.1: Extensively studied Ising like magnetic materials. The last column indicates the separation between the ground and first excited states in the energy scale of $k_b T_c$. Adapted from [17]

For a couple of these materials we present measurements of specific heat, magnetization and magnetic susceptibility contrasted with theoretical predictions.

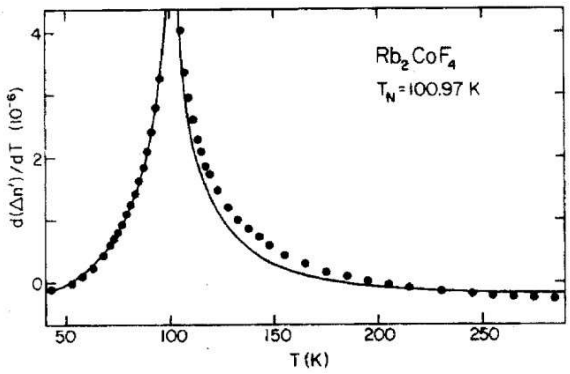

Figure 4.2: Variation of the magnetic specific heat, as a function of temperature for Rb_2CoF_4 . The solid points (o) are experimental results of optical birefringence measurements shown previously to be proportional to the magnetic specific heat. The solid line is the exact Onsager solution for the two-dimensional Ising model with amplitude and critical temperature adjusted to fit the data, and a small constant background term subtracted. Adapted from [17]

The strinking similarity between theoretical predictions and experiment inspired more and more research in the last century. A lot of new experimental tools and mathematical approaches stemmed from from this cooperation, one pushing the other to their limits, which is exactly what doing science should be. As a byproduct, new magnetic behaviors were discovered, in evidence the effects of frustration which we now brief.

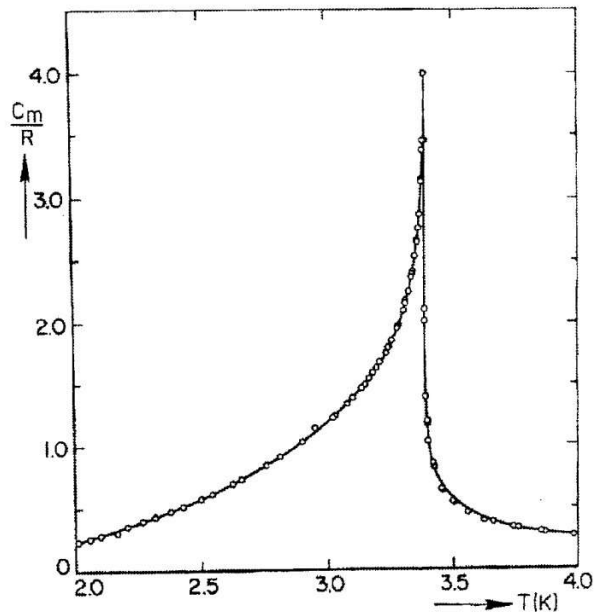

Figure 4.3: Magnetic specific heat as a function of temperature for DyPO4. The points (o) represent experimental results, the solid line represents the results of a calculation based on high- and low-temperature series expansions with one adjustable constant. Adapted from [17]

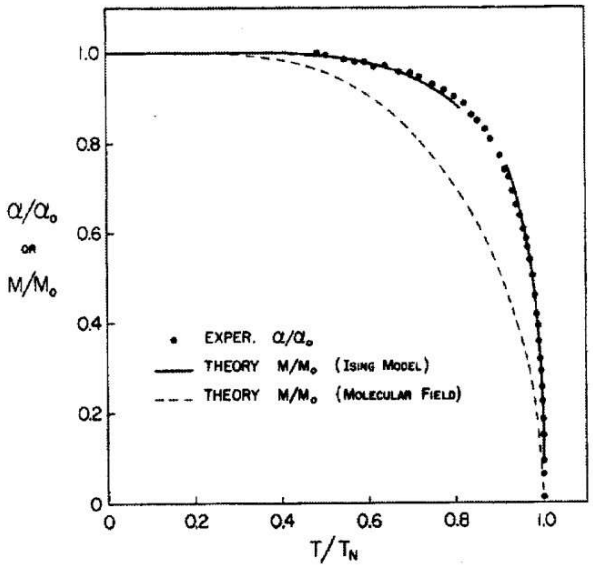

Figure 4.4: Spontaneous sublattice magnetization as a function of temperature for DyPO4. The points (o) represent experimental results of magneto-electric measurements; the two solid lines represent the results of a calculation based on a low- temperature series expansion with one adjustable constant, and a fitt to a power law with a fitted critical exponent $\beta = 0.314$. The broken line represents the molecular field theory. Adapted from [17]

4.2 Spin Ice

In 1935 Pauling noted that tetrahedral ice structures have macroscopically degenerate ground states. This is due to the fact that in a cell, the two hydrogen atoms of a molecule are closer to the central oxygen than the other two hydrogens in the same cell which come from other molecules. This causes the dipole in each interaction to point either inward or outward and as the system grows, the number of ways in which this happens grows exponentially. An analogous situation arises in tetrahedral Ising spin lattices. In this case the effects of geometrical frustration occur if there is a ferromagnetic coupling, meaning all spins wish to point inward for example. Figure 4.5 ilustrates the situation

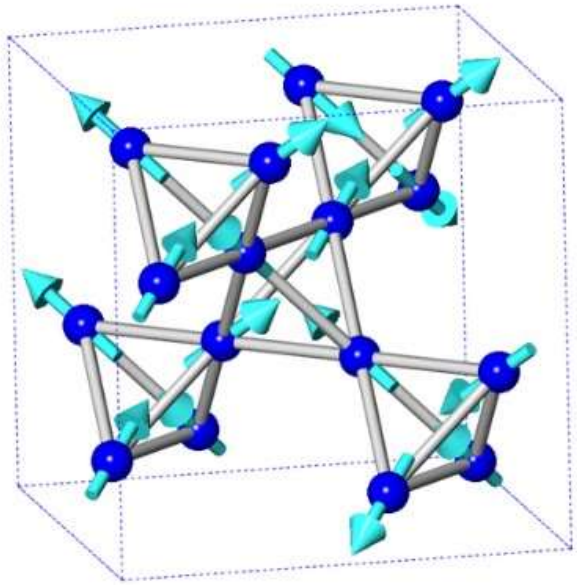

Figure 4.5: A schematic representation of the pyrochlore lattice, showing the positions of the magnetic ions. Adapted from [18]

Reference [17] mentions a study with the al $Dy_2Ti_2O_7$ pyrochlore, asserting that two different monte carlo simulations of this system predicted its spin ice properties which were later confirmed by experiments, emphasizing the role of computer simulations in guiding experiment. Figure 4.6 ilustrates one of the results. Once again, the agreement between simulation and experiment is remarkable and motivates me to further pursue this field of study.

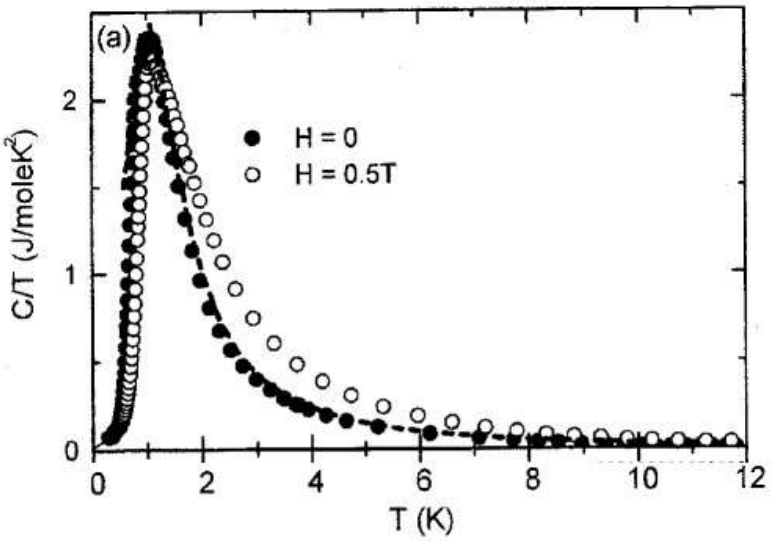

Figure 4.6: Specific heat and entropy of $Dy_2Ti_2O_7$. The dashed line is Monte Carlo simulation of the zero field C(T)/T.Adapted from[17]

Chapter 5

Machine Learning and Artificical Inteligence

In this chapter we lay out the core ideas behind machine learning (ML) and describe the two main distinct approaches to analyse data with it, supervised and unsupervised learning. Good references are [19] and [20]

5.1 Supervised Learning

Before going into algortithms and techniques we are going to discuss the shift in perspective with respect to a what a computer program is brought to light by ML concepts.

In traditional programming loosely speaking we have a set of rules which are implemented through loops and conditionals to perform a certain task. For instance, one could acquire crystalographic data and wish to identify the inner structure of a material. You could feed the data to a program consisting of orientation and symmetry criteria which will then spit an output : FCC, BCC, etc.

The shift in perspective comes when we don't know the criteria themselves and they become the object of study. Suppose we don't know what a BCC nor a FCC structure is, but the same material has different mechanical properties depending on different external parameters, such as pressure and temperature, and given a crystalographic sample we wish to find out what microscopic feature sets them appart. One could then feed this data to a ML algorithm with a label, 0 or 1 for simplicity, depending on which mechanical

properties they correspond to. The procedure to make a ML code learn is yet to be described, but the gist is that you force it to make a decision: such data either belongs to the 0 *class* or 1. In the begining of a training process, the outcome is random, but our ML structure is penalized for making mistakes, and forced to adjust its parameters taken into account in the decision making process in a direction such that if it sees another sample with similar properties it will have a higher probability of making the right choice.

In the end of this training process we are expected to have the set of rules which identify correctly different crystal structures. They may be purely abstract or interpretable, they may coincide with previously known criteria or not. The finding of these criteria is the main reason why ML is useful in physics: Most interesting phenomena are not well understood, so we can ask for machines to learn them and then try to interpret the results. This is precisely the aim of this thesis.

Neural Networks for classification

The intent of this subsection is to be informal and not technical. The only intent is to be clear on *how* and *why* neural networks can perform any task at all.

The introductory example is to classify written digits in the 10 different $(0, 1, 2, 3, 4, 5, 6, 7, 8, 9)$ classes. We start by apprecating how hard it would be to find criteria to identify these digits, fig 5.1, based on pixels.

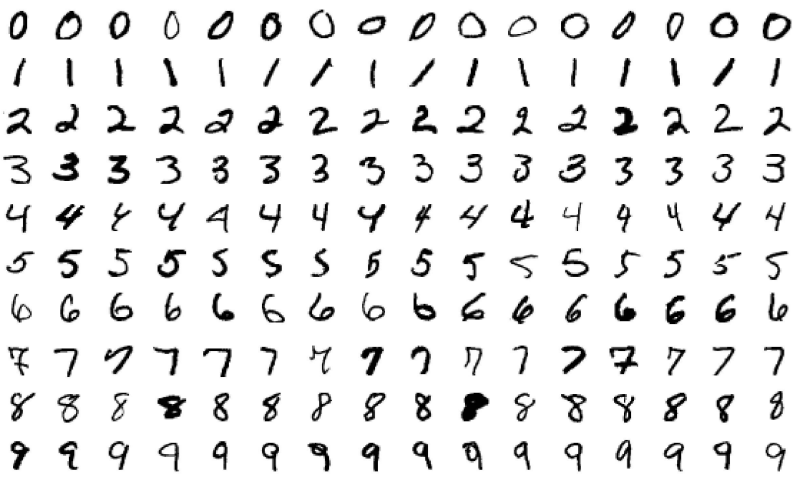

Figure 5.1: Sample of famous Mnist dataset consisting of handwriten digits. Adapted from [21]

Now we define the structure in fig 5.2. It consists of an input vector $\vec{x}$ of size equal to the number of pixels in the image, and each layer is a vector of some size. The input vector will be forwarded to a hidden layer by multiplying it by a weight matrix $\boldsymbol{W}$ plus a bias vector $\vec{b}$. Finally the values stored in the hidden vector are each the result of applying an activation function f to the previous operation. This process is repeated until we get to the output vector which is a probability of pertaining to each class.

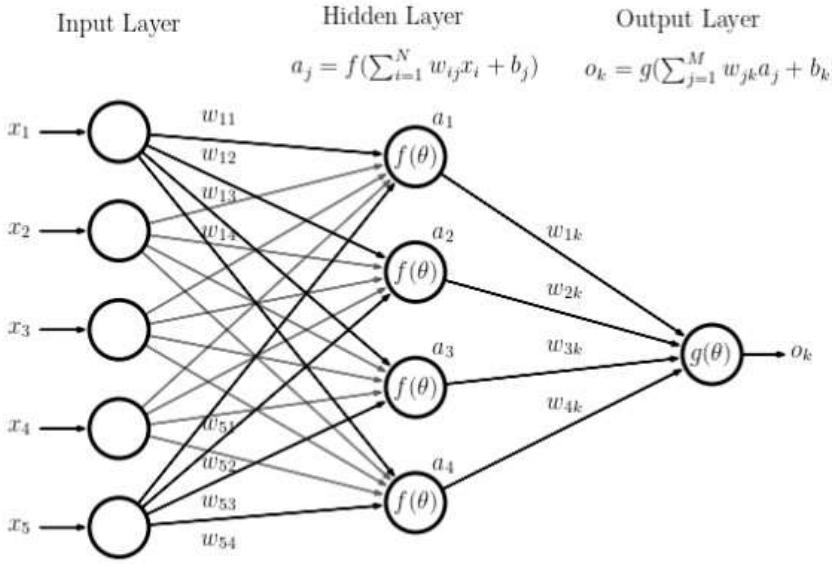

Figure 5.2: Structure of fully connected Neural Network. Adapted from [22]

As this process a priori has no reason to spit reasonable answers, we have to analyze the error in the answer by comparing to the correct probability vector (zeros in all but the true class).

The error function, for example, root mean square error, is a function of all parameters in the network, of all terms in all the $\boldsymbol{W}$ matrices and $\vec{b}$ vectors. Each one of them can therefore be tuned by gradient descent in a notoriously complex process called backpropagation. Once we reach a (hopefully) global minimum we can stop.

The last paragraph sheds light on what the *learning* in ML means. Learning is an optimization process in the space of parameters with respect to the error function, as depicted in fig 5.3.

In practice the optimization process learns a decision boundary, or threshold, in feature space which best splits regions of feature space into belonging to either class. The boundary is a manifold in feature space.

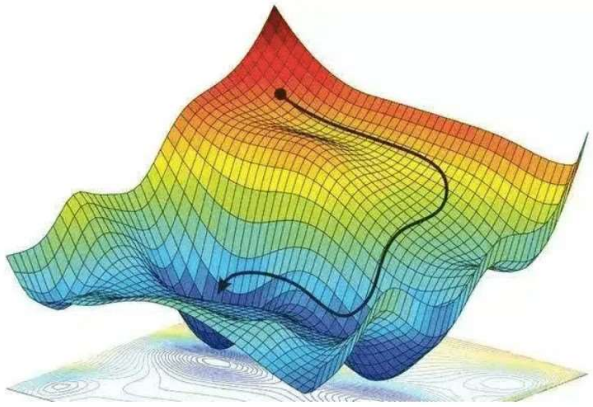

Figure 5.3: Literally the learning path. Adapted from [23]

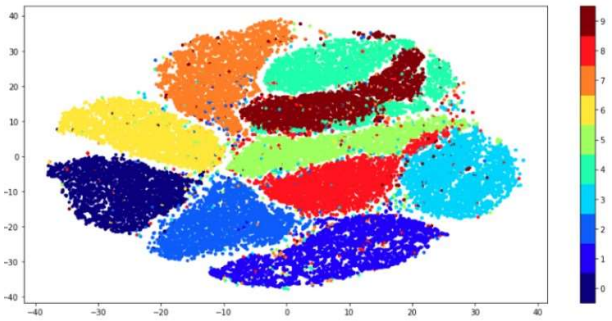

Figure 5.4: T-SNE projected Mnist dataset labeled by colors. A classification task on this dataset would aim to find the best possible curves that separate reagions of each class. Adapted from [24]

The process would for example try to separate the plane in fig5.4 into regions of only one color

Referring to the last section, we did not know what set of for's, if's and else's to implement in order to identify whether an image was a zero or whatever. Now we still don't know, but the neural network does. We could try to rationalize what the NN is doing but most of the time it is a black box. Interpretability in deep learning is an active area of research and we have attempted it succesfully in

As a final remark, the size of each hidden layer, which activation functions to use where, the number of layers, etc are all free parameters which have great impact on the success of the structure as a whole. This is where practice and experience in building them come in to the scene.One interesting results is that the deeper the NN, meaning the more layers it has, the more nonlinearities it can capture.

The example discussed here is the simplest possible which will encompass the essence of deep learning. Our discussion could get as complex as desired and it is not

desired to develop the theory of deep learning in this thesis, but merely to discuss every necessary topic to understand the data analysis process present in ref.[16], so now we move on to unsupervised learning.

5.2 Unsupervised learning

The second main approach to ML is unsupervised learning, which consists of searching structure in unlabeled data.

Dimensionality Reduction: PCA

High dimensional data is notoriously difficult to annalyze. For instance, in any image the number of pixels is the dimension of the data. We therefore ask the question: Can any low dimensional representation of the data preserve core information about the real data?

The answer is: sometimes. But it is yes often enough to motivate a lot of research on how to proceed effectively. The first method presented is called Principal Component Analysis, or PCA. To ilustrate the procedure, let us analyse figure 5.5, in which a toy dataset is plotted deliberately adding random disturbances (left) in the direction normal to the plane (right).

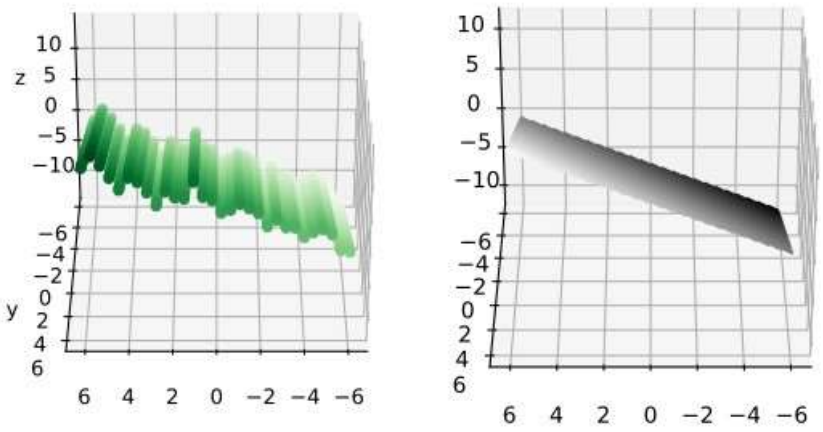

Figure 5.5: Toy dataset to ilustrate PCA

This is intentionally done to lead you into believing a two dimensional representation of the inherently three dimensional data to the left reasonably captures its nature. In practice, with a dataset of arbitrary dimension we can't tell whether it could be reasonably represented by far lower dimensions, cutting computational costs and hopefully even providing a faithful 3d visualization. PCA is a procedure in which we build the covariance matrix of the data, and since it is symmetric, it is diagonalizable. We then

find its eigenvectors and eigenvalues, which are orthogonal. The eigenvectors are called principal components and are ordered by drecreasing magnitude of the eigenvalue. In covariance matrices the eigenvalues represent the amount of variance in the eigenvector direction. The higher the variance of the data in a direction the more important it is to *explain* the data. Hopefully it is clear in our example the very low variance normal to the plane, leading to eigenvectors which would span the plane.

Let us not loose sight of the physical applications of ML, namely PCA has been used to identify order parameters in phase transitions for they contain information about stable phases.

PCA is very usefull as a first approach and test, but one shortcoming is the inherently linear nature of the procedure. To show you why this would be a problem, imagina a three dimensional helix on the surface of a cylinder. Intrinsically it is one dimensional, therefore is parametrizable by one parameter. PCA cannot deal with it.

Dimensionality Reduction: Autoencoders

At the supervised learning section we teased the solution to the PCA inherently linear nature. Neural networks capture nonlinearities easily as we increase the number of layers in the structure, as we see see in fig 5.6, so we are motivated to reduce dimensionality

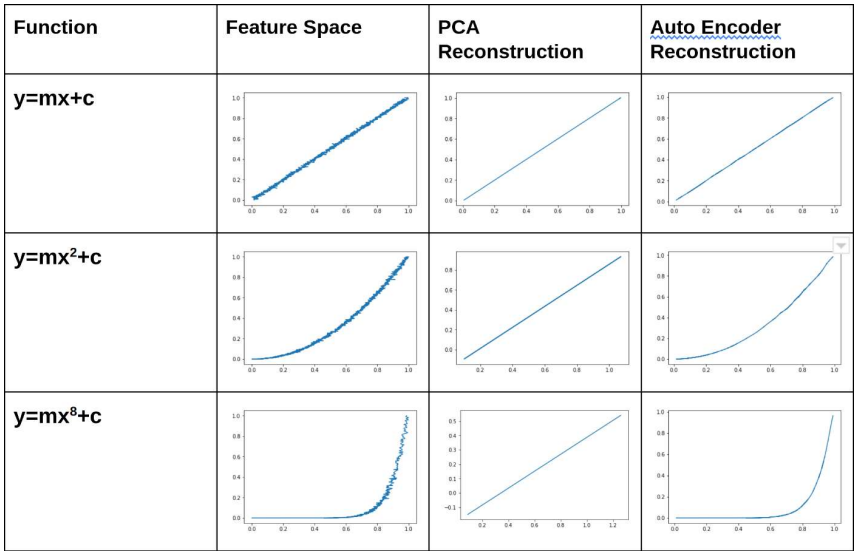

Figure 5.6: Data reconstruction from PCA and Autoencoder. The Autoencoder is capable of capturing nonlinearities. Adapted from [25]

via neural networks. Now arises the question: how to adapt the forementioned optimiza-

tion process of classification of digits to our problem? Unsurpisingly, Autoencoders are neural networks.

The idea is to build a neural network aimed at reproducing the input with a bottleneck layer in the middle, compressing and decompressing the data. The "zipped" data is often called latent representation, for in low dimensional space we force the NN to find latent features which underlie the structure of the data, extracting what is essential to recover it, as in fig5.7.

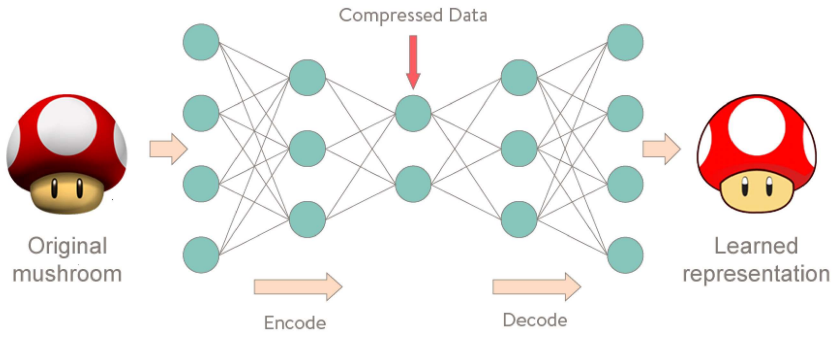

Figure 5.7: Architecture and functionality of Autoencoders. Adapted from [26]

Autoencoders are fascinating objects with numerous applications. For example, noise is deffinetely not essential to describe data, so autoencoders are often used as filters, as in fig 5.8

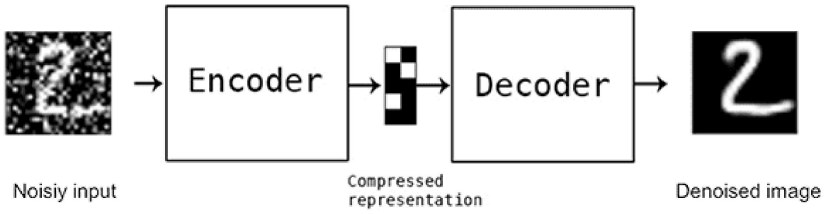

Figure 5.8: Autoencoders used for denoising. Adapted from [27]

In my paper I have discussed the relationship between the number of degrees of freedom in a physical system and the dimension of latent space. It turns out, in our study, that the minimum dimension necessary for recovery is the number degrees of freedom of the partition function.

It is worth noting the loss of order of importance, in contrast with PCA in which the eigenvectors are ordered by magnitude of the eigenvalue. Instead, we check the reproduction error to assess the quality of the latent manifold.

Clustering

Finding reliable low dimensional representation of data can be very insightful, providing clues on the instrinsic structure of the dataset as a whole. In clustering the aim is now to find latent *substructures* in the dataset, subsets with common characteristcs. We proceed by choosing a metric with respect to which individual samples can be considered close or far appart. The notion of distance in the dataset, just as the choice of an error function in NN's, is always crucial to a meaningful outcome of our method, and data exploration can be done prior to applying any method to help in the choice.

Clustering is a more arbitrary task than any other exposed here in that it is not clear what we want to achieve, nor if it even makes sense to search for subgroups within a general dataset. Each dataset is very unique in this sense and needs to be assessed case by case.

Figure 5.9 displays the outcome of different clustering approaches to the same datasets.

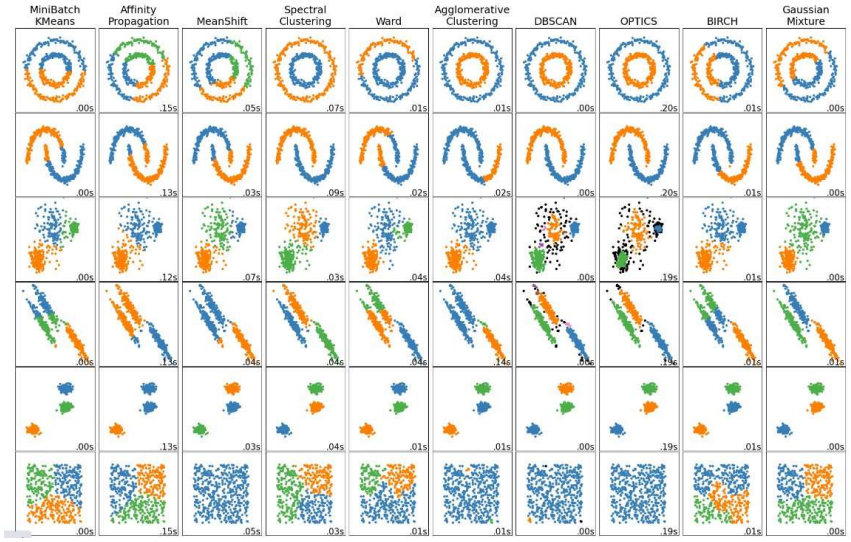

Figure 5.9: Various clustering procedures applied to different datasets yielding differnt outcomes. Adapted from [28]

It is very difficult to measure the quality of a clustering result. For instance, consider the bottom left corner image. Kmeans consists of finding n optimal "centers of mass" recursevely starting from random initial conditions, taking n as an input. It will always converge even if there is no structure to be found. In contrast, now focusing on the top left corner, KMeans does find a meaningful substructure, a symmetry axis

of the data. Now, looking at the data it is easy to realize there is a more interesting substructure waiting to be identified, the concentric rings. DBSCAN, on the other hand, does find this inner structure for it clusters by density, searching for at least n neighbours in a given ϵ radius, as depicted in fig 5.10, being able to find clusters of arbitrary shape

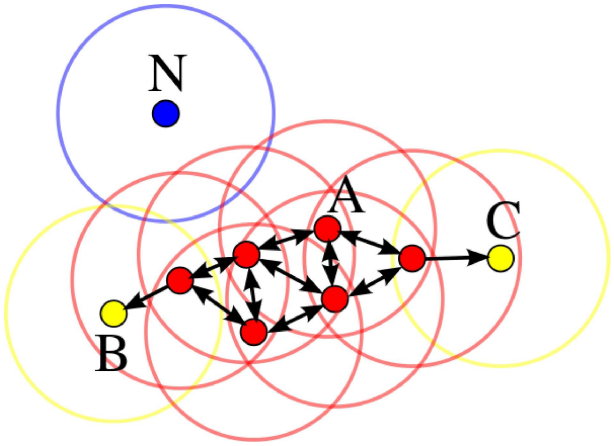

Figure 5.10: The DBSCAN algorithm works by searching for n, n=3 in this picture, neighbours in a given radius. If the condition is met, the data is considered a core sample (red), if it isn't but it is contained in a neighbourhood of a core sample it is an edge sample (yellow). If none is met, then it is considered noise (blue). Adapted from [29]

given that data are "linked" by these neighbours. It is also robust to noise, disregarding "anomalous" data which shouldn't be part of any cluster at all.

In this example maybe it seems that we should always use the DBSCAN method, but let us not loose sight of the fact that these are toy datasets, and, even worse, two dimensional. The task of measuring the quality of any given clustering outcome is not simple and is subject of intense research. Some standard methods are the silhouette coefficient, which measures the average distance of each data within a cluster and contrasts it with the average distance to all other clusters, somewhat defining a notion of uniformity within a cluster, or a silhouette. Other would be to analyze the density profile of the dataset prior to clustering, computing a distance matrix from each data point to its firt neighbour and verifying the existence of a characteristic density. Keep in mind that computing either the silhouette coeficient or the density profile implies defining a metric in feature space. This is highly nontrivial, specially if the features are categoric (color of the eye, for example).

All the ideas necessary for understanding ref [16] are now at the table. My intention in writing is such that reading this thesis thoroughly will provide a completely self contained account of the published article in Physica A. With nothing but a minor pause

we can proceed to the paper.

Chapter 6

Machine Learning Phase Transitions

The seminal paper in this field of study is [30] and was the main inspiration for this study. Either in it or in the supplemental material, the authors apply all the techniques presented in this thesis to various spin systems. It demonstrated the power of pattern recognition of ML in phase transitions and teased the new insights it could provide. It certainly instigated me to deeply study and dedicate myself to make a contribution.

The Ising Model has always fascinated me in a personal level, for it has been so exhaustively examined and is still able to provide so much insight, linking different areas and presenting a plethora of behaviours.

The main takeaway from my paper[16], in the next section, is the power of ML when applied to systems which we know nothing about. We could either gather experimental data or define a Hamiltonian and hit play in monte carlo, then apply ML techniques to unveil not only phases but fundamental properties of the system, such as order parameters, degrees of freedom of the partition function, symmetry etc.

Before actually presenting it I would like to summarize the article to make it more digestible. I perform single spin flip monte carlo to both the PUD an ZZD models at a set of random coupling constants. I apply a cooling protocol starting from a region which is definetely paramagnetic, the only stable phase I allowed myself to assume, for at high enough temperature *any* system is an ideal gas. Having reached whatever state it got through this very slow cooling procedure (seeking global minima), I save one sample. That is done such that every sample analyzed is absolutely uncorrelated to any other sample.

This is the data acquisition process stemming from monte carlo. Next, dimensionality reduction is achieved through different means, namely PCA and Autoencoder, yielding different results. PCA leads us into a discussion about order parameters, while the Autoencoder latent spece is far richer, exibiting features related to macroscopic degeneracy , hamiltonian symmetry and, in envidence, degrees of freedom.

Next I cluster the latent space data (following a rigorous optimization procedure) and map the produced clusters into the $(\tilde{J}, T)$ space from which the parameters of the simulation were first uniformelly sampled. In this space the clustered samples form clear distinct regions, which we assign classes to and perform classification on. The decision threshold between classes is in great quantitavely agreement with the analytical solution for phase boundaries in both models.

We conclude by recalling the difficulty in simulating frustrated spin systems, and after this difficulty is overcome, the difficulty in analyzing the data. Frustration is a very relevant phenomenom and this pipeline of machine learning techniques combined with monte carlo data can provide reliable insight into the thermodynamics, degrees of freedom, entropy, symmetry and order parameters of the system under study.

It is important, I feel, to make it clear what the role of ML in physics is. It is a toolbox of pattern recognition techniques which may come in handy. It is not suitable for extremely precise estimates, such as critical exponents. Rather, when very little is known, the best direction towards which scientists should direct their efforts, such as "*what region do I analyze with greater resolution*?", can be indicated through ML techniques.

I am excited to explore the possibilities further, but for now I am very proud of the work I have done and I hope you have learned something in reading this. Now to the paper.

Chapter 7

Global exploration of phase behavior in frustrated Ising models using unsupervised learning techniques

7.1 Introduction

Over the past few years machine learning (ML) has revolutionized the way in which the behavior of complex systems is investigated, providing a data-driven approach that exploits the pattern-recognition powers of such techniques [19]. In particular, it has had a tremendous impact on the physical sciences, where ML methods have been applied to a wide variety of problems originating from areas as diverse as condensed-matter and statistical physics, particle physics, cosmology, quantum computing, chemistry and materials science [31].

Within the field of condensed-matter physics, a major purpose of the application of ML techniques has been to discover the phase behavior of different physical systems [30, 32–50]. In this context, a variety of classical spin systems [30, 32, 34, 35, 40, 45, 46, 51–54] have played a particularly prominent role, displaying the promise of ML techniques

in the discovery of complex phases of matter from raw sampling data.

In practice, many of these applications have focused on examining phase behavior as a function of a single parameter, often temperature, seeking to characterize transitions for given fixed values of possible other model parameters. Such an approach has shown to be successful, for instance, to quantify particular critical-temperature values in a number of such spin systems [30, 32, 33, 54].

A different kind of application of ML techniques is to employ their pattern-recognition capabilities to gain insight into a system's *global* phase behavior. In this case, instead of focusing on a single critical value for a restricted set of parameter values, the purpose now is to analyze a data set consisting of configurations generated for the full system parameter space, with the goal of estimating entire critical lines and constructing a picture of the phase diagram as a whole. Such a capability is useful, for instance, when no *a priori* insight into the location of critical regions is available. Casert and co-workers [33] employed such a scheme for the active Ising model, constructing gas-liquid coexistence lines in the density-temperature parameter space. Their approach is based on a two-step procedure in which unsupervised learning techniques are first used to determine phase boundaries for a fixed value of the density, followed by a supervised learning step in which phase boundaries can be predicted for different densities. Acevedo *et al.* [34] reconstructed the critical line between the antiferromagnetic and paramagnetic phases of the two-dimensional frustrated antiferromagnetic Ising model on the honeycomb lattice using anomaly detection [55] based on convolutional autoencoders. For this purpose, they trained an autoencoder on temperature-dependent data for a particular fixed value of the frustration coupling constant and then used it to analyze data generated for other values to detect the transition between ordered and paramagnetic phases using anomaly detection.

In the present paper we consider a different global learning approach in which a single unsupervised learning procedure based on dimensionality reduction is applied to a data set containing samples generated for the entire parameter space. Moreover, these configurations correspond to random parameter values so as to obtain an unbiased data set, presuming no prior knowledge of the system. As an illustration, we construct the phase diagrams of two classical lattice spin systems involving several parameters, namely, the piled-up dominoes (PUD) and zig-zag dominoes (ZZD) models. These models were introduced in the 1970's as generalizations of the totally frustrated 2D Ising model [56] and incorporate effects of geometrical frustration by the existence of two different spin-

spin coupling-parameter values distributed according to regular patterns on the 2D square lattice. The phase behavior of these models is nontrivial, depending on both temperature as well as the relative values of the two coupling constants. In particular, the PUD model displays three types of second-order phase transition: two of them occurring at finite temperature between a paramagnetic phase and either a ferromagnetic or striped antiferromagnetic phase, and a third featuring a transition with vanishing critical temperature.

We analyze the raw Monte Carlo (MC) spin-configuration data generated for randomly selected points in the models' parameter spaces by means of a three-stage data approach that consists of, (i) dimensionality reduction using principal-component analysis (PCA) and auto-encoders, (ii) clustering using the density-based spatial clustering of applications with noise (DBSCAN) algorithm, and (iii) classification using a support-vector machine (SVM). The obtained results enable us to construct the critical lines of the PUD and ZZD models and, given the availability of exact results for both systems, the quality of these estimates can be assessed.

The remainder of the manuscript has been organized as follows. In Sec. 7.2 we define the PUD and ZZD spin-model Hamiltonians and describe the geometric distribution of the two coupling-parameter values across the 2D square lattice. Subsequently, we discuss the details of the employed methodology in Sec. 7.3, describing the MC procedure employed to generate the set of spin configurations used in the analysis, as well as the ingredients of the ML approach used to process the data. The results are presented and discussed in Sec. 7.4 and we end with concluding remarks in Sec. 7.5.

7.2 Models

As for the standard 2D square Ising system, the PUD and ZZD models are defined by classical spins $s_i = \pm 1$ arranged on a square lattice with nearest-neighbor interactions. However, unlike the standard Ising model, the PUD and ZZD models are characterized by varying interaction-strength parameters. Specifically, the total energy of both models can be written as

$$H = -\sum_{\langle ij \rangle} J_{ij} s_i s_j, \tag{7.1}$$

where i and j label the spin sites, the notation $\langle ij \rangle$ implies a summation over nearest-neighbor spin pairs and J_{ij} is a spin-pair-dependent interaction-strength parameter with

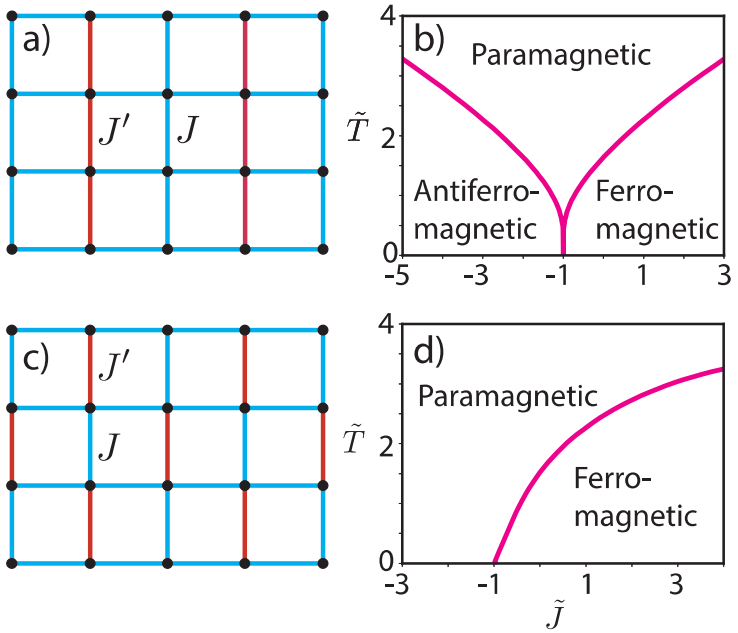

Figure 7.1: Definition of spin-interaction patterns in, a), the piled-up dominoes (PUD) model and, c), zig-zag dominoes (ZZD) model. Black circles represent spin sites. Blue and red links represent interactions with strengths J and J', respectively. Corresponding exact phase diagrams characterized by critical lines given by Eqs. (7.2) and (7.3) are depicted in b) and d), respectively.

the dimensions of energy. For the PUD and ZZD models J_{ij} can assume only two values, J and J', which can be either positive or negative. In addition, their distribution across the 2D square lattice is specified in a geometrically ordered pattern, as illustrated in Fig. 7.1. All horizontal spin pairs interact through the coupling parameter J. In contrast, the interaction parameter J' couples only spin pairs that are *vertical* neighbors, but only a limited set of them, with the remainder being coupled by J. Specifically, for the PUD model, J' acts on all pairs of alternating vertical rows, as shown in Fig. 7.1 a), meaning that all spin pairs in even (odd) vertical rows interact through J', whereas all pairs in the odd (even) vertical rows are coupled through J. In the ZZD model, on the other hand, the interaction between spin pairs from the vertical rows alternates between J and J' and such that neighboring vertical rows are "out of phase", creating the zig-zag pattern depicted in Fig. 7.1 c). Given the structure of the Hamiltonian in Eq. (7.1) the phase behavior of both models can be characterized entirely in terms of the two adimensional parameters $\tilde{J} \equiv J'/J$ and $\tilde{T} \equiv k_B T/J$, with T the absolute temperature and k_B Boltzmann's constant. Of course, both models reduce to the standard 2D square Ising model for $\tilde{J} = 1$. Furthermore, for $\tilde{J} = -1$, the models correspond to the fully frustrated Ising model [56]. Their phase behavior is known exactly, as displayed in Figs. 7.1 b) and d). Specifically, the PUD model features three distinct phases, paramagnetic, anti-

ferromagnetic and ferromagnetic, separated by continuous phase transitions described by two critical lines that are solutions of the equations

$$\sinh\left(\frac{2}{\tilde{T}}\right)\sinh\left(\frac{1+\tilde{J}}{\tilde{T}}\right)=\pm 1, \tag{7.2}$$

respectively, with the minus sign corresponding to the left branch. The ZZD model, on the other hand, is characterized by paramagnetic and ferromagnetic phases, separated by the critical manifold given by the solution of the equation

$$2\tanh\left(\frac{2}{\tilde{T}}\right)\tanh\left(\frac{1+\tilde{J}}{\tilde{T}}\right)=1. \tag{7.3}$$

Interestingly, the disordered paramagnetic phase persists up to zero temperature for values of $\tilde{J}$ below -1.

7.3 Methodology

7.3.1 Data Generation

The parameter space of the models is sampled randomly, employing uniform distributions for the parameters $\tilde{J}$ and $\tilde{T}$ within the intervals $\tilde{J}\in(-3,1)$ and $\tilde{T}\in(0,3)$ for the PUD model and $\tilde{J}\in(-3,3)$ and $\tilde{T}\in(0,4)$ for the ZZD system. To this end we fix $J=1$ and sample J' and T according to the established intervals. Subsequently, for each randomly chosen pair $(\tilde{J},\tilde{T})$, we record a single representative spin configuration, generated as follows. After initializing the system in a random spin configuration it is subjected to a process in which it is cooled starting from a predefined high temperature, $T_0=5$, down to the sampled target temperature $\tilde{T}$. This particular value of T_0 has been chosen to assure that, for any parameter sample $(\tilde{J},\tilde{T})$, the generation process initializes in the same disordered paramagnetic state common to all Ising-like spin system, minimizing bias in the data set.

The cooling protocol is implemented using standard single-spin-flip Metropolis Monte Carlo (MC) simulations [57] in which the temperature T is reduced at a rate of 2×10^{-4} per MC sweep, which is defined as a set of N random spin-flip trials such that, on average, each of the N spins in the system is given the opportunity to alter its

state. After the cooling stage is completed, the system evolves isothermally at the target temperature $\tilde{T}$ for an additional 3×10^3 MC sweeps, after which the final configuration is recorded in the data set. Since only a single configuration is registered for each randomly sampled parameter pair $(\tilde{J}, \tilde{T})$, all collected spin configurations are statistically independent.

7.3.2 Data-analysis

Our data-analysis strategy to estimate the critical manifolds is based on three elements. First, we subject the raw MC configurations to unsupervised-learning techniques with the aim of achieving dimensionality reduction of the data. In addition to having shown to be effective in capturing essential features of physical systems [35, 40], from a data-analysis standpoint it is useful for tackling difficulties associated with the high-dimensional nature of the raw data set [58]. Next, we process the reduced-space results using clustering algorithms [59] to identify distinct groups within the data. In some situations dimensionality reduction alone suffices to identify different groups within the data set, but in more complex scenarios, such as in this study, this is not the case. Either way, clustering techniques should be applied to the reduced space so that the identification of coherent groups is unbiased. After this clusterization we map the elements of the identified clusters to the phase diagram using the values of the parameters $\tilde{J}$ and $\tilde{T}$ associated with each data point and verify whether the distinct agglomerates are located in different regions, to be interpreted as distinct phases. Finally, we use the labels generated by the clustering procedure to train a classifier and interpret the obtained decision thresholds in terms of the critical manifolds. Below we describe the details of each of the three elements, all of which have been implemented using the `Scikit-learn` platform [60].

Dimensionality reduction

We apply two different approaches for the dimensionality reduction step, using both principal-component analysis (PCA) [61, 62] as well as develop an auto-encoder [63]. PCA achieves dimensionality reduction by determining the eigenvectors, also known as principal components, of the covariance matrix of the raw MC data (with dimensions $N \times N$, with N the number of spins in the system). The principal components (PCs) are then ranked in order of decreasing eigenvalues. The first eigenvector (i.e., that with the

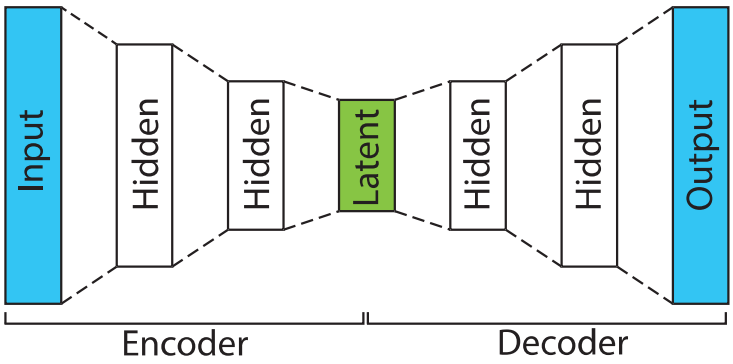

Figure 7.2: Hourglass structure of auto-encoder neural network. Each block represents a set of neurons. Number of neurons in input and output layers equals the dimension of the data set. Starting from the input layer, the subsequent hidden layers systematically reduce the number of neurons until reaching the bottleneck latent neuron block in which the number of neurons reaches a minimum. Subsequently, the Intermediate, hidden layers, systematically reduce the number of neuron until reaching the latent neuron block in which the number of neurons reaches a minimum. Part between the input and the latent block is referred to as the encoder. Part between the latent block and output is referred to as the decoder.

largest eigenvalue) corresponds to the high-dimensional direction in the spin space that has the largest variance in the data set. Subsequently, the second eigenvector corresponds to the direction with the second-largest variance, and so on. The assumption then is that only a few PCs are sufficient to capture the essential information contained in the data set and, possibly, also allowing to group them. A restriction of the PCA approach, however, is that it is a fundamentally linear operation, excluding the possibility to detect non-linear relationships among the variables in the data set.

Auto-encoders, on the other hand, allow detection of such non-linearities. They are neural networks which take the elements of the data set as input and are trained to reproduce that input in the output layer. The structure is that of an hourglass, as shown schematically in Fig. 7.2. Starting from the input layer, with a number of neurons equal to the dimension of the data set, each subsequent hidden layer decreases its number of neurons until reaching the latent neuron block, which is the layer with the fewest neurons. This part of the structure is referred to as the encoder. The other part of the hourglass is known as the decoder, in which the number of neurons in the hidden layers increases again, in a manner symmetric to the encoder part, until reaching the original number of neurons in the output layer. The dimensionality reduction of the data is achieved by the encoder part, with the bottleneck layer spanning the so-called latent space, which represents a nonlinear distilled representation of each input sample.

Compared to PCA, which amounts to applying a straightforward linear transformation to the data, the creation of an auto-encoder is much more involved. In addition to specifying the number of layers in the hourglass structure and the number of neurons in each of them, including the minimum number of neurons of the latent space, it requires the definition of the neural network. This entails defining the connectivity between the layers, the weights of the connections between the neurons and the functional forms of the activation functions.

Clustering

Among the many available clustering techniques [59] we use the density-based spatial clustering of applications with noise (DBSCAN) algorithm [64]. This choice is motivated by a number of arguments. First, it does not require to pre-define the number of clusters as input. Moreover, it is well-suited to handle noisy datasets and, as opposed to the vast majority of clustering methods, it can identify groups with arbitrary shape. The main principle of the DBSCAN approach is to group together data points that lie within a neighborhood of a specified radius ε. In particular, it searches for those data points that, within this neighborhood, have a specified minimum number of neighbors. Each point that satisfies this criterion is classified as a core point. If a data point does not satisfy this property but it is part of the neighborhood of a core point it is considered a border sample. Finally, if none of these conditions are met, the data point is considered noise.

Classification

Finally, after the clusterization step, we apply a classification approach to determine the boundaries between different clusters. To this end we use a support-vector machine (SVM) [66], which provides a robust method for determining nonlinear and fuzzy intersections between clusters.

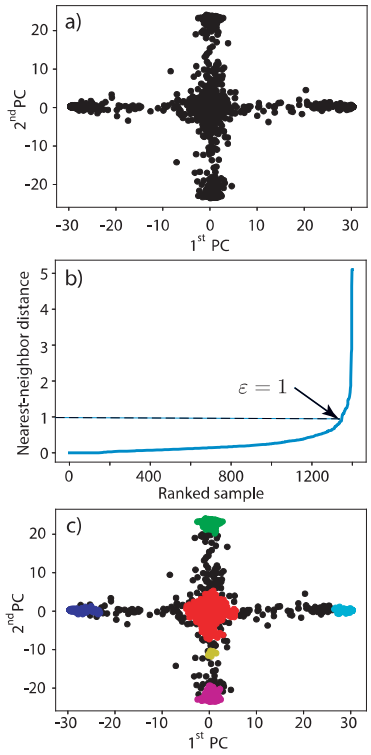

Figure 7.3: PCA dimensionality reduction of the MC data for the PUD model followed by clustering using DBSCAN. a) Projection of the data on the space spanned by the first 2 PCs. b) Nearest-neighbor distance for each data point in this space, ranked from the smallest to largest. Arrow indicates the location of maximum curvature, which has been shown to provide an appropriate value for the nearest-neighbor radius parameter ε for the DBSCAN clustering algorithm [65]. c) Results after clustering. Black circles represent data points classified as noise. Different colors correspond to data points attributed to distinct clusters.

7.4 Results and Discussion

The main results for the PUD model are based on a data set containing 1400 independent spin configurations on a 30×30 2D square lattice subject to periodic boundary conditions, each obtained for a single, uniformly sampled parameter pair $(\tilde{J}, \tilde{T})$, as discussed in Sec. 7.3.1. Figure 7.3 a) displays the results obtained after a dimensionality reduction using PCA, with each data point representing one of the 1400 spin configurations as projected on the two-dimensional space spanned by the first two PCs. Next, to apply the DBSCAN clustering approach, we first need to select an appropriate value for the neighborhood radius parameter ε. To this end, we analyze the distribution of nearest-neighbor distances in PCA-reduced space depicted in Fig. 7.3 a). Figure 7.3b) plots the value of this nearest-neighbor distance for each data point, ranked from lowest to highest. It has been shown [65] that the optimal value of ε corresponds to the distance at which the curvature of the distance versus rank curve is maximum, which in this case

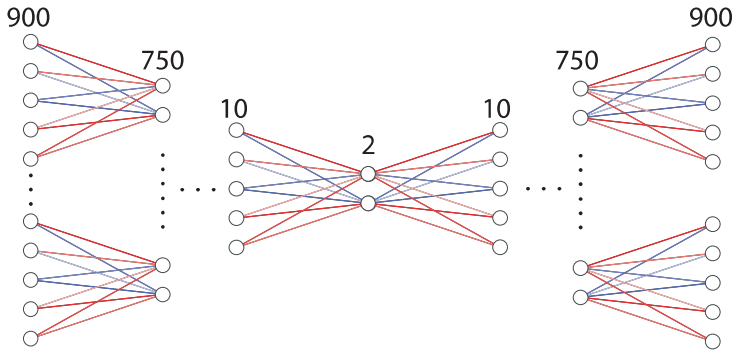

Figure 7.4: (Color online) Artificial neural network structure of auto-encoder. In addition to the input layer consisting of 900 neurons, the encoder portion consists of 8 hidden layers with, respectively, 750, 600, 450, 300, 150, 75, 30 and 10 neurons, before reaching the latent layer containing 2 neurons. The decoder portion is symmetric with respect to the latent layer. The neural network is linked such that subsequent layers are fully connected.

is $\varepsilon \simeq 1$, as indicated by the arrow. Figure 7.3 c) then shows the results after clustering with DBSCAN, using a neighborhood radius $\varepsilon = 1$ and setting the minimum number of neighbors within this radius to be 10. Aside from the black circles, which are configurations that have been classified as noise, the data points painted with different colors belong to distinct clusters.

As a second approach toward dimensionality reduction we develop an auto-encoder with the schematic structure shown in Fig. 7.2. The resulting optimized neural-network structure is depicted in Fig. 7.4. In addition to the 900 neurons on the input layer, the encoder section features a succession of 8 hidden layers with, respectively, 750, 600, 450, 300, 150, 75, 30 and 10 neurons, before reaching the latent layer that consists of 2 neurons. The decoder part is symmetric with respect to the latent layer. The neural network between successive layers is fully connected and we employ hyperbolic tangents as activation functions [58]. The optimization of the auto-encoder neural network was implemented using the `PyTorch` package [67], employing its MSELoss function as the loss measure and the Adam algorithm as the adaptive optimizer. The optimization process is organized in three steps. First, the auto-encoder is pre-trained using 400 of the 1400 system configurations at a learning rate of 5×10^{-4} for 1500 iterations (i.e., epochs). Subsequently, the training procedure covers the entire data set for 4000 more iterations using the same learning rate. Finally, an additional 2000 iterations is carried out for the entire data set at a learning rate of 5×10^{-5}. The corresponding dimensionality-reduced representation of the data set is shown in Fig. 7.5 a), which depicts the outputs of the neurons L_1 and L_2 of the latent layer for the 1400 spin configurations. Subsequently, to

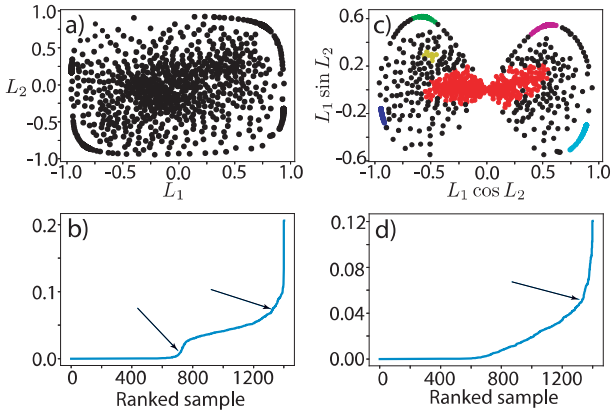

Figure 7.5: Auto-encoder dimensionality reduction and subsequent DBSCAN clusterization for the PUD data set. a) Data represented in the latent space as characterized by the output L_1 and L_2 of the corresponding 2 neurons. b) Cluster density analysis based on ranked nearest-neighbor distances for data points shown in a). c) Transformation of the latent space in terms of the transformed variables $L_1 \cos L_2$ and $L_1 \sin L_2$, respectively. Different colors represent data points in distinct clusters as obtained using DBSCAN. Black circles indicate configurations classified as noise. d) Cluster density analysis based on ranked nearest-neighbor distances for latent-space points shown in c).

determine the value of the radius parameter ε for DBSCAN, we determine the nearest-neighbor statistics of the data set in the same way as done in Fig. 7.3 b).

The results are shown in Fig. 7.5 b), which shows the nearest-neighbor distance for all data points in Fig. 7.5 a), ranked from lowest to largest. The fundamental difference between this profile and the one obtained for PCA is that, in this case, there are two local maxima in the curvature of the the rank-distance plot, as shown by the arrows. This indicates that groups belonging to the latent space as represented in Fig. 7.5 a) have different characteristic densities. The existence of two density profiles can in fact be traced to the physical characteristics of the PUD model, as we will discuss later on, but under these conditions the DBSCAN clustering algorithm is known to be less effective. If one chooses ε according to the smaller of the two, i.e., focusing predominantly on clustering data points characteristic of high density regions, lower-density samples will not be recognized as belonging to any group at all. In contrast, if we select the larger of the two, i.e., choose cluster according to lower density regions, regions of higher density will incorporate data points that should not be included, giving rise to cluster overlap.

In this case, it has been shown that a transformation of coordinates in the latent space may be helpful to improve the identification of distinct clusters. Specifically, polar-coordinate-like interpretations have shown to particularly useful on a number of occasions, including in the recognition of handwritten digits [68–70]. Following this approach, we

transform the neuron outputs L_1 and L_2 of Fig. 7.5a) by interpreting L_1 as a generalized "radius" (allowing both positive and negative values) and L_2 as an "angle", giving new Cartesian components defined as $L_1 \cos L_2$ and $L_1 \sin L_2$, respectively. Inverting the roles of L_1 and L_2 in this transformation does not alter the results. Figure 7.5 c) and d) display the corresponding structure of the transformed latent space and rank-distance curve, respectively, with the latter now having a single point of maximum curvature, allowing an effective application of the DBSCAN clustering algorithm. As in Fig. 7.3 c), the different colored data points in Fig. 7.5c) correspond to distinct clusters identified by DBSCAN, whereas the black circles correspond to configurations that are classified as noise.

Having clustered the data for both dimensionality-reduced representations, we now map the corresponding spin configurations onto the $\tilde{T} \times \tilde{J}$ parameter space of the PUD model, maintaining the color coding adopted in Figs. 7.3 c) and 7.5 c). The corresponding results are depicted in Figs 7.6 a) and b), which display the mappings produced by PCA and the auto-encoder, respectively. An immediate observation is that, in both cases, each non-noise color occupies only a restricted part of the parameter space, dividing it into three distinct regions. Figure 7.6c) shows representative spin arrangements from these areas, clearly showing the distinct nature of the spin conformations in each of them. In this sense, each region represents a distinct spin phase, displaying a disordered paramagnetic phase, a ferromagnetic phase and a stripe-like anti-ferromagnetic phase. A further notable feature of the data mapping in Fig. 7.6a) and b) is that, while the paramagnetic region corresponds to a single cluster, the ferro and anti-ferromagnetic parts of the parameter space are occupied by two distinct clusters each. We will further discuss this point below.

Now that the various clusters in the dimensionality-reduced spaces of PCA and the auto-encoder in Fig. 7.6 have been associated with different types of spin configurations, we now analyze the data so as to determine the manifolds in the parameter space that separate the different phases. To this end, we define three different classes, corresponding to the three regions in the parameter space identified in Fig. 7.6 a) and b). In particular, the classes consist of, (i), the spin configurations from red cluster for the paramagnetic phase, (ii) the data from the light and dark blue clusters for the ferromagnetic phase and, (iii), the green and magenta clusters for the stripe-like anti-ferromagnetic phase. Based on these classes we employ a supervised-learning SVM multi-classification approach to establish the boundaries between these regions. The corresponding results for PCA and the auto-encoder are shown in Fig. 7.7 a) and b), respectively. The different background

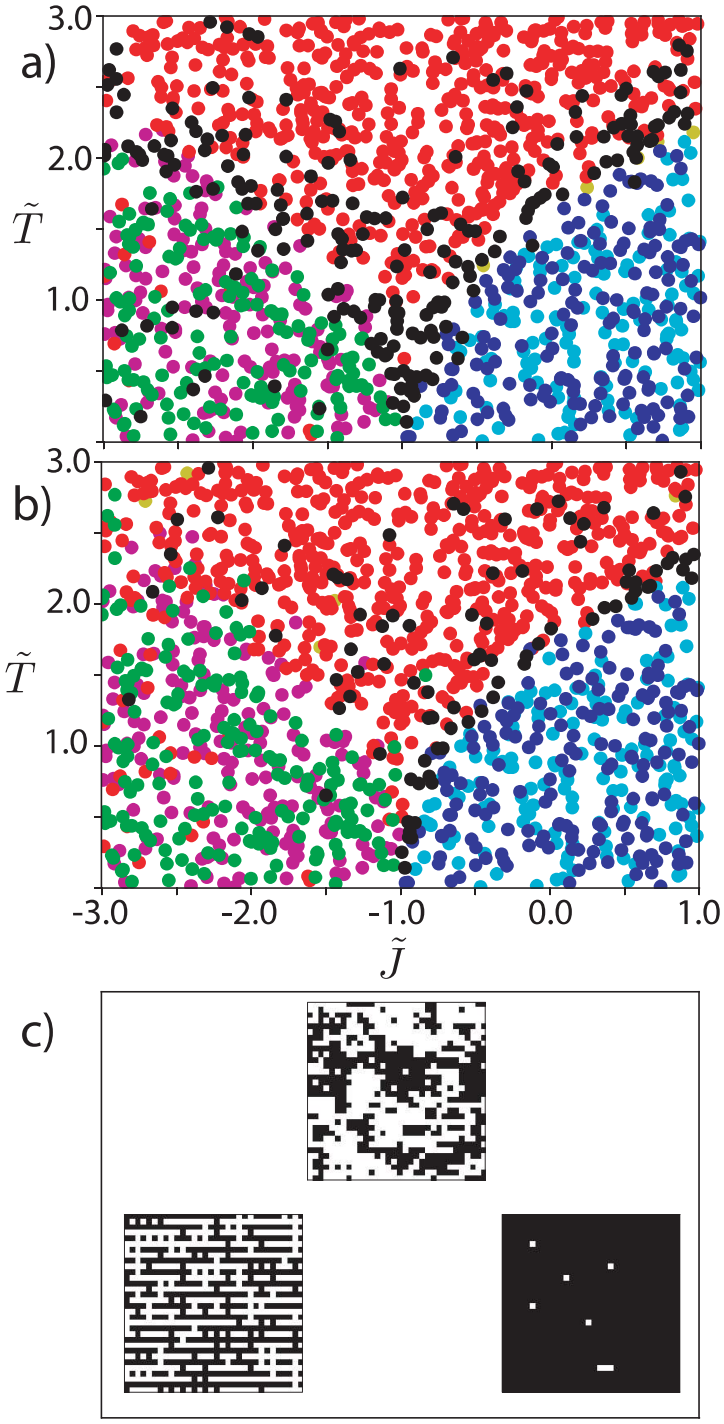

Figure 7.6: (Color online) Mapping of reduced-space clusters into the PUD parameter space. a) PCA clustered data. b) Auto-encoder clustered data. c) Representative spin configurations for the three phases with black/white squares representing spin up/down, respectively.

colors correspond to the different classes, with the boundaries between them representing the so-called decision thresholds that form the critical manifolds in the parameter space that separate the different phases. We can compare these results directly to the critical lines defined by Eq. (7.2), shown as the dashed white lines.

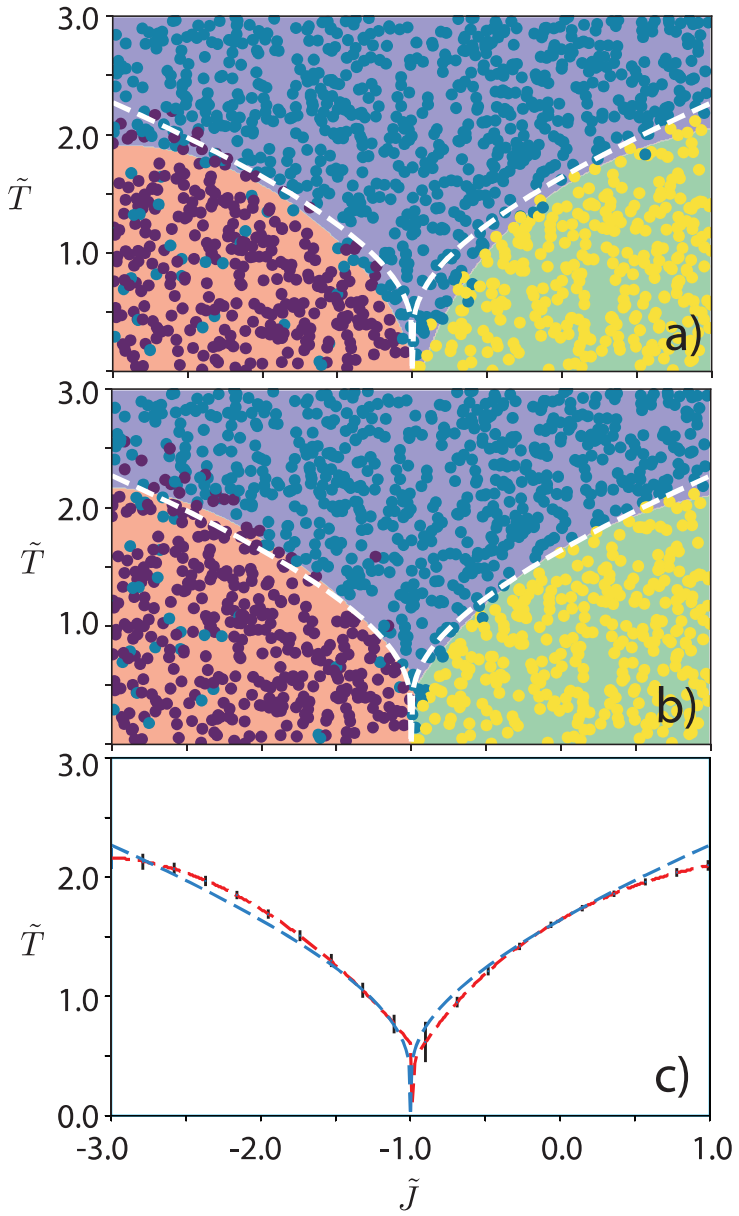

Figure 7.7: (Color online) Colored circles represent the spin configurations after DBSCAN clustering of the PCA and auto-encoder dimensionality reduction. Dark and light blue data points in Fig. 7.6a) and b) have been assigned to the yellow circles, the green and magenta to purple, and the red and black to blue. Different background colors represent regions defined by the SVM as belonging to a specific class. The boundaries between them represent the decision thresholds. White dashed lines represent analytical critical lines corresponding to the solutions of Eq. (7.2). a) PCA-based phase diagram. b) Polar-coordinate latent-space phase diagram from auto-encoder. c) SVM decision threshold (red line) including uncertainty estimates (vertical black bars) as estimated using the train-test split method [60] compared to analytical critical lines (blue line).

Overall, both PCA and the auto-encoder closely capture the qualitative features of the critical lines in the parameter space, including the existence of a critical point at zero temperature for $\tilde{J} = -1$. It is clear, however, that the phase-behavior description provided by the auto-encoder is superior in terms of quantitative agreement, with

the SVM decision thresholds closely overlapping the analytical results. This is further demonstrated in Fig. 7.7 c), which compares the SVM decision thresholds including confidence intervals as obtained using the train-test split method [60], to the exact results. The agreement is encouraging, in particular because the data points were selected randomly and uniformly within a very broad range of the parameter space, without any bias toward known transition lines.

The main reason for the quantitative difference between PCA and the auto-encoder is the fact that the first 2 PCs cover only 34% of the variance in the data, with the remaining 66% being diluted over the other 897 eigenvectors. The auto-encoder, on the other hand, provides a more comprehensive data reduction scheme. Although it does not involve the concept of explained variance, as for PCA, the fidelity obtained in training the auto-encoder can be used as a measure for the accuracy in the recovery of the input image by the encoder. In this particular case, the auto-encoder can be pushed to reproduce input images with a fidelity superior to 90%. As discussed previously for a variety of other classical spin systems [32, 34], the superiority of the auto-encoder approach is not surprising given that PCA is intrinsically limited to linear transformations of the data.

Even so, the PCA dimensionality reduction, followed by DBSCAN clustering still provides insightful information regarding the physical characteristics of the system. In particular, it has been shown to be useful in the identification of order parameters characterizing phase transitions [32, 71]. This can be appreciated in the cluster structure depicted in Fig. 7.3 c), in which vertically and horizontally opposite clusters belong to the same striped anti-ferromagnetic and ferromagnetic phases, respectively, whereas the centralized red agglomerate corresponds to the paramagnetic phase. In this sense, the first PC clearly distinguishes between the two symmetric ferromagnetic states (i.e., spin up and spin down) and the paramagnetic phase, whereas the second PC does so to differentiate the (spin-up and spin-down) striped anti-ferromagnetic phases from the paramagnetic phase.

Fig. 7.8 shows the results obtained for the other frustrated spin system, defined by the ZZD model, which is characterized by a different geometric patterns of the coupling parameters J and J'. The dimensionality reduction is obtained using an auto-encoder with the same two-neuron bottleneck architecture applied for the PUD model. Fig. 7.8 a) displays the resulting latent-space structure after applying the same polar-coordinate-like transformation used for the PUD model and using DBSCAN clusterization. It displays the same butterfly-like shape as for the PUD, but in this case the number of distinct clus-

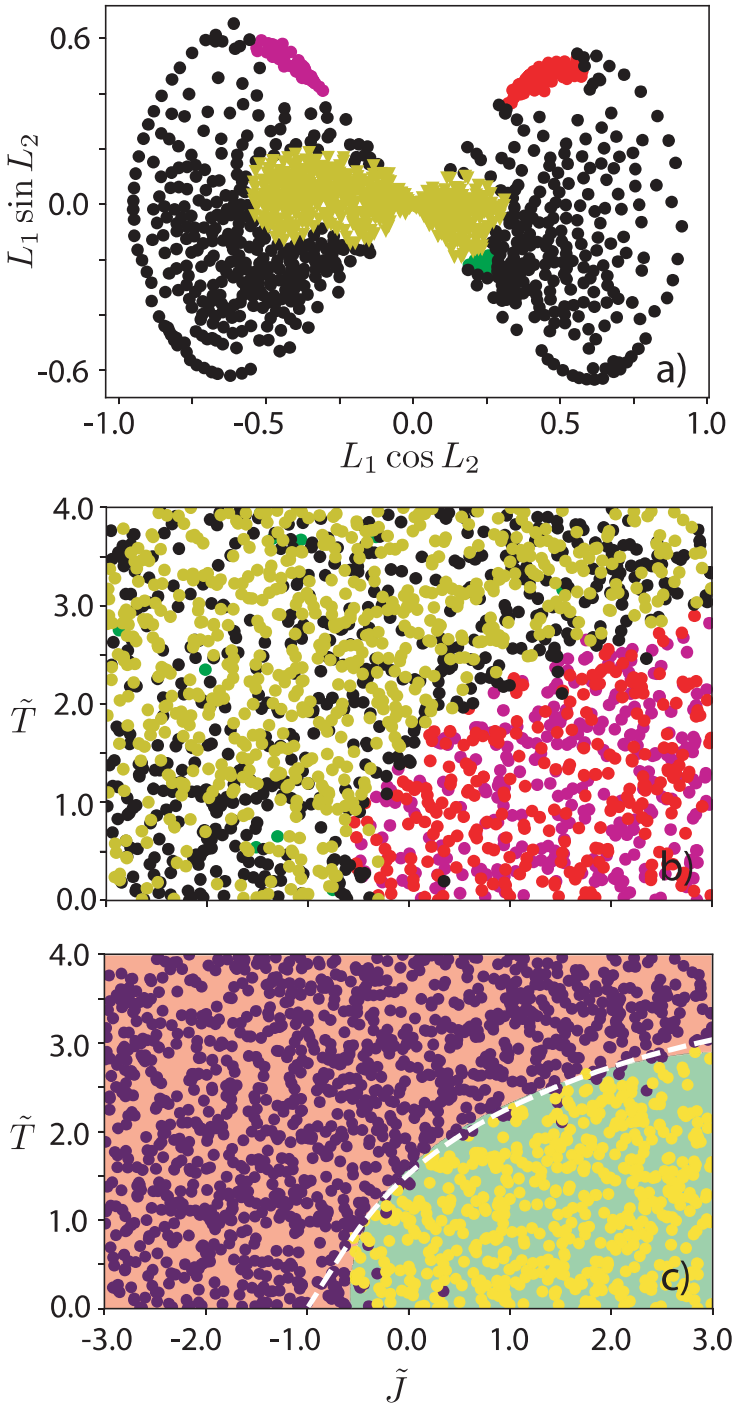

Figure 7.8: (Color online) Auto-encoder results for ZZD model. a) Hyperspherical latent space after DBSCAN clustering, with different clusters represented by different colored circles. b) Spin configurations plotted in the $(\tilde{J}, \tilde{T})$ parameter space, maintaining the colors from a). c) Corresponding ZZD phase diagram as obtained by SVM classification. Different background colors represent regions defined by the SVM as belonging to a specific class. The boundaries between them represent the decision thresholds. White dashed line represents analytical critical line from Eq. (7.3).

ters is reduced by two. Specifically, the two mirror-symmetric clusters on the lower part of the butterfly for the PUD model have disappeared. When mapping the data points onto

the $(\tilde{J}, \tilde{T})$ parameter space, as depicted in Fig. 7.8 b), it is clear this reduction is related to the fact that the ZZD model is characterized by two instead of three phases, displaying a ferromagnetic phase for positive values of $\tilde{J}$ and low $\tilde{T}$ and a disordered paramagnetic phase for negative values of $\tilde{J}$ or high temperatures. After grouping the clusters belonging to the same region of the phase diagram into distinct classes and training an SVM classifier we obtain the critical line separating both phases as the boundary separating both background colors, as shown in Fig. 7.8 c). As for the PUD model, the agreement with the exact result described by Eq. (7.3), shown as the white dashed line, is excellent.

An interesting question is to what extent there is a relation between the structural characteristics of the optimized auto-encoder and the fundamental physical characteristics of the two spin models. In this context, we note that for both spin models the best results are obtained using a bottleneck layer formed by 2 neurons, obtaining a reproduction fidelity $\gtrsim 90\%$. If, for instance, only a single neuron is used, the optimized fidelity does not exceed $\sim 50\%$, whereas a bottleneck layer containing three neurons does not significantly improve the fidelity. The fact that the optimal latent-space dimension is two for both systems, even though the number of distinct phases for both models is different (3 for the PUD versus 2 for the ZZD), suggests that the optimal dimension of the latent space may be related to the number of independent parameters required to characterize the phase diagram. A further indication for the connection between the structure of the auto-encoder latent space and the physical characteristics of the system can be seen in Figs. 7.5 c) and 7.8 a). The butterfly-shaped hyper-spherical latent spaces are mirror-symmetric with respect to the vertical axis passing through the origin, with the symmetry-related cluster pairs belonging to the same regions in the phase diagram. The symmetry brought out by the clustered auto-encoder results thus provides insight into the physical system under consideration, revealing that opposite clusters contain configurations that are spin reversals of each other. In other words, the vertical axes in Figs. 7.5 c) and 7.8 a) correspond to the spin-reversal symmetry underlying the system Hamiltonians. This "discovery" of a fundamental system symmetry through the optimization of the auto-encoder is a further example that the global ML phase exploration employed here can be useful in perceiving fundamental properties of physical systems when prior theoretical insight is unavailable.

In a similar context, the existence of two density profiles in the Cartesian auto-encoder latent space for the PUD model, as shown in Fig. 7.5 b), is in fact related to the nature of its ferro and antiferromagnetic phases of the PUD model. Theoretical analysis

indicates that the entropy of its anti-ferromagnetic phase is much greater, meaning that the variability among different samples is much larger compared to that for the ferromagnetic configurations. This is the reason underlying the existence of the two density profiles for the ranked sample-sample distances in Fig. 7.5 b). Whereas the clusters belonging to the lower ε (i.e., higher density) correspond to ferromagnetic configurations, the ones for the larger ε value represent anti-ferromagnetic spin conformations. Even though the data does not allow quantification of the configurational entropy for both phases, it does provide qualitative indications that it is larger for the striped anti-ferromagnetic phase, without previous knowledge of the system.

It is interesting to contrast the present fully-connected auto-encoder approach to that employed for the two-dimensional frustrated antiferromagnetic Ising model as reported in Ref. 34. In the latter, a convolutional auto-encoder (CAE) was used to determine the critical line between the antiferromagnetic and paramagnetic phases. The advantage of CAEs over the fully connected auto encoder utilized in the present work is that they are characterized by a much smaller number of parameters and feature the ability to recognize spatial correlations by the application of filters or local transformations on the images, allowing, for instance, to construct the phase diagram of the Bose-Hubbard model [72]. Even so, in addition to the fact that the implementation of CAEs is generally substantially more involved, the CAEs in Ref. 34 do not have a low-dimensional latent space, such that its detection of phase transitions is not based on dimensionality reduction, but rather on anomaly detection. In this sense, both auto-encoder techniques approach the construction of phase diagrams in very different manners and may be considered as complementary to each other. Particularly useful features of the present fully-connected auto-encoder approach are its interpretability in terms of the latent space features and its efficiency, giving accurate estimates for the critical lines based on only 1400 MC spin configurations.

A final point concerns the influence of the system size on the global estimate of phase diagrams. In applications of ML techniques used to locate a single critical point, such a size-dependence analysis has been instrumental in achieving quantitative accuracy [30, 32]. In the context of classical spin systems, for instance, such an analysis involves generating configurations in the vicinity of a critical point for different linear lattice dimensions L, after which pertinent outcomes are analyzed as a function of some power of L. For instance, using PCA for the standard 2D ferromagnetic Ising model, its critical temperature can be determined by plotting the temperature for which the

quantified second principal component reaches its maximum as a function of L^{-1}, followed by extrapolation to the limit of infinite lattice dimension [32].

In the present global ML approach, however, in which one uses a single data set consisting of configurations sampled from the entire parameter space of the system, local scaling properties become blurred. First, the dimensionality reduction encodes the characteristics of the phase diagram as a whole, incorporating a continuum of critical temperatures instead of a particular single value. Furthermore, in a similar fashion, the final estimates for the critical lines are obtained using a SVM classifier, whose result corresponds to the minimum of a classification error that is global in nature rather than reflecting behavior in the vicinity of a single critical point. This is illustrated in Fig. 7.9, which displays the PCA results for the PUD model for lattice dimensions $L = 8,\ 16$ and 64. The size effect on the distribution of the data points in the clustered latent space is evident. Whereas the results display appreciable dispersion for $L = 8$, the projections onto the first two principal components become progressively sharper as the system size grows, increasing the distinguishability among the ferromagnetic, anti-ferromagnetic and paramagnetic phases. On the other hand, even though the SVM critical lines for $L = 64$ are visibly better than those obtained for $L = 8$ in an overall sense, there is no manifestly visible size-scaling behavior. This is shown in the inset of Fig. 7.9 f), which plots the SVM critical temperature as a function of $1/L$ for the case of the standard 2D Ising model (i.e., $\tilde{J} = 1$). Even though the estimates are within 7% of the exact value for all system sizes, there is no discernible L^{-1} dependence.

In this sense, the present global ML approach can be considered to be complementary to the schemes that have been utilized to quantify the parameters characterizing a particular critical point [30, 32]. Whereas the present approach allows one to obtain a good first picture of the overall phase diagram when no *a priori* insight is available, the latter can subsequently be used to systematically obtain better accuracy for the critical parameters by targeting the generation of additional data in the vicinity of the initial transition estimate and using techniques as described in Refs. 30 and 32. This is also consistent with the findings of Théveniaut and Alet for the many-body localization transition in the Heisenberg spin 1/2 chain [53], who reported that uncertainties in the estimates for critical parameters extracted from neural-network structures tend to be larger than those obtained from conventional approaches.

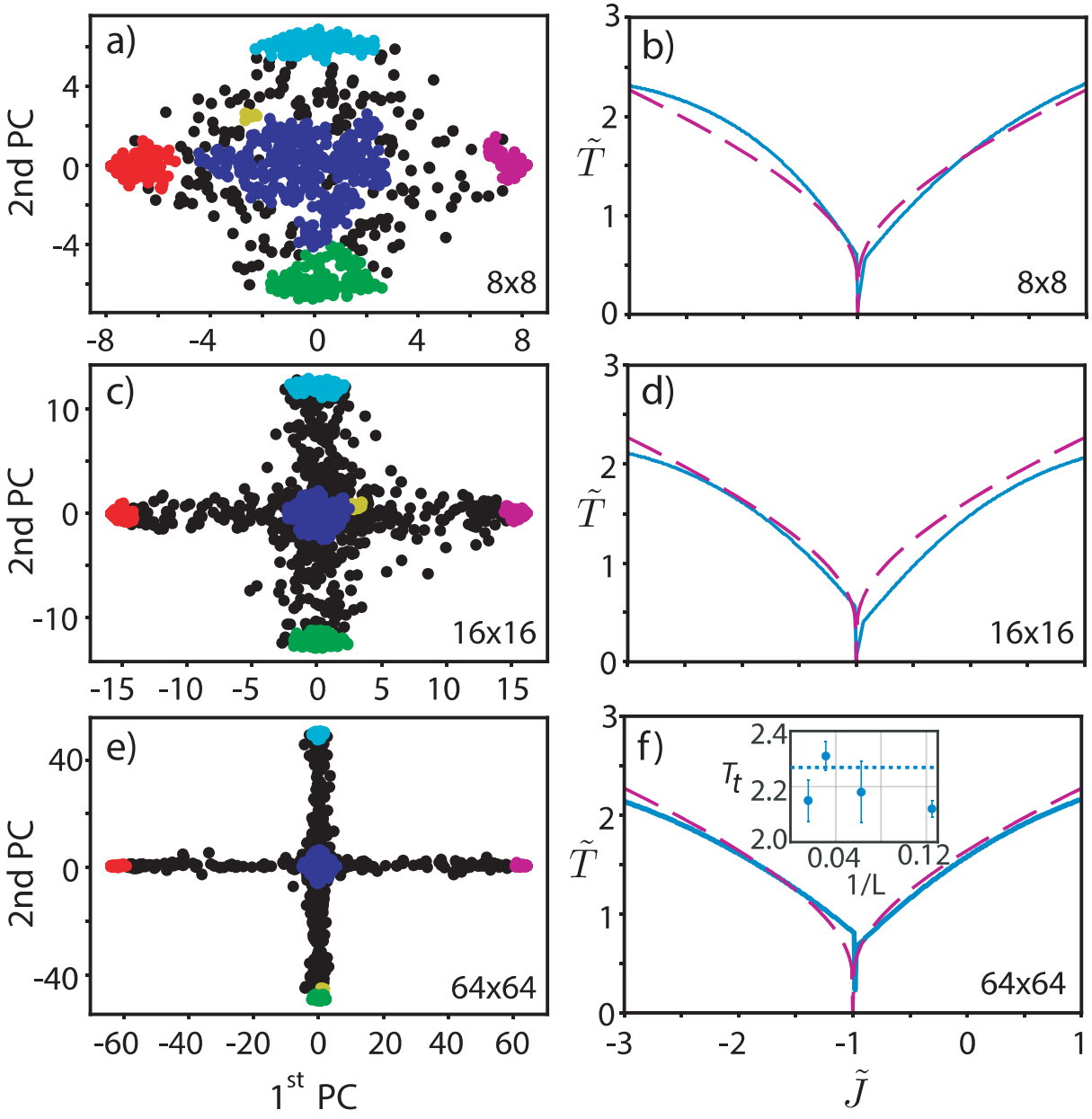

Figure 7.9: (Color online) System size dependence of latent space and corresponding SVM estimates for the critical lines for PUD model for 8x8 16x16 and 64x64 lattice sizes. Inset in f) displays SVM critical temperature estimate as a function of L^{-1} for $\tilde{J} = 1$, with horizontal dashed line indicating exact value $T_c = 2/\ln(1+\sqrt{2})$.

7.5 Conclusions

In summary, we consider a ML approach for obtaining a global prediction of the phase diagrams for two frustrated Ising models, which are characterized by the presence of critical lines rather than a single critical point. Using raw MC spin configurations generated for random parameter values from the entire parameter space, we first apply unsupervised learning techniques such as PCA and auto-encoders to achieve dimension-

ality reduction, followed by clustering using the DBSCAN method and a classification step using a SVM approach. The resulting estimates for the critical lines of both systems are in excellent agreement with available exact results, even though the data points were selected randomly and uniformly within an ample region of the parameter space, without any predisposition toward the critical lines.

In both cases, the auto-encoder dimensionality-reduction approach is found to provide better quantitative results as compared to those based on PCA. The main origin of this difference is that the optimized auto-encoder gives an image fidelity $\gtrsim 90\%$, with two neurons in the bottleneck layer. In contrast, the corresponding two-dimensional latent space for PCA captures only 34% of variance in the data. A further observation is that the latent-space characteristics of the optimized auto-encoders appear to relate to fundamental physical characteristics of both considered spin models. In addition to recognizing the spin-up/spin-down symmetry, in both cases the best results are obtained using a bottleneck layer formed by 2 neurons, indicating that the optimal latent-space dimension is linked to the number of independent parameters required to characterize the phase diagram. Although this relation between the optimal auto-encoder structure and the physical properties requires further study, it suggests that the present ML approach may be helpful in perceiving fundamental physical properties when, for instance, *a priori* theoretical insight is unavailable.

Finally, although the approach provides good estimates for the phase diagram as a whole, it is not naturally suited to be used in finite-size scaling procedures that are often employed to accurately quantify critical parameters. This is due to the fact that the predictions are based on data sets generated for the entire parameter space rather than in the vicinity of a particular critical point. In addition, the estimates for the transition lines are obtained using a classification procedure that seeks to minimize a global classification error across the phase diagram as a whole such that local critical properties become obscured by global optimization criteria. In this sense, the present approach is complementary schemes that are utilized to quantify critical parameters by focusing on data generated in the vicinity of a critical point.

CRediT authorship contribution statement

D.R.A.E: Conceptualization, execution of computations, writing. E.G: Conceptualization, review and editing. M.K.: Conceptualization, writing and supervision.

Declaration of competing interest

The authors declare that they have no known competing financial interests or personal relationships that could have appeared to influence the work reported in this paper.

Acknowledgments

The authors acknowledge support from CNPq, Fapesp grants no. 2016/23891-6 (MK) and 2018/19586-9 (EG), as well as the Center for Computing in Engineering & Sciences - Fapesp/Cepid no. 2013/08293-7 (MK). We gratefully acknowledge Rodolfo Paula Leite, Levy Boccato, Romis Ribeiro de Faissol Attux and Gabriel Reis Garcia.

Chapter 8

Conclusions and Future perspectives

In this chapter we summarize the main results and conclusions from this Thesis. We also present an future perspectives and research directions based on the results obtained in this thesis.

8.1 Conclusions

In the course of my graduate studies I have learned thoroughly the theory of second order phase transitions, from analytical tools to numerical simulation, focusing on the latter. The conventional 2D Ising model hs been scrutinized to a great extent, including renormalization group analysis as well as single spinf flip and cluster monte carlo algorithms. Comparisons on the physical interpretation of the algorithms' dynamics, both qualitative and quantitative, shed light on the nature of the phase transition and emphasize the collective and continuous behavior of the system. Two critical exponents were found using finite size scaling techniques, and the remaining were found using the scaling relations derived via renormalization group analysis.

Next the concept of frsutration and it's relevance for modern physics is discussed. We present the most relevant model for this thesis, the PUD model, and present an analytical technique, the transfer matrix, to extract exact conclusions about its ground state. After discussing the ZZD model, we present experimental results contrasted to the theory of Ising models to emphasize the relevance of the theoretical studies and advances in this field.

The second main subject of this thesis is machine learning, so we present the main concepts and ideas through examples. First supervised learning is discussed through the lenz of neural netorks for classification, where the learning path is understood to be the decision error minimization in parameter space via gradient descent. Next, unsupervised learning is discussed and the exmples given are dimensionality reduction and clustering. Two examples of dimensionality reduction are presented, PCA and autoencoder, and their differences emphasized, namely the linearity versus nonlinearity of the methods. Next, the idea of clustering is presented and contrasted to the task of classification, and the interpretability and quality assessment issues are strongly emphasized.

The thesis wraps up by presenting our published paper, which combines the techinques and concepts of all previous chapters to uncover the stables phases present in both the PUD and ZZD models, as well as presenting interpretability of machine learning techinques which correlate to physical features of the system.

8.2 Future perspectives

Succeding the studies discussed and reported here, we suggest the following research directions to explore:

- Extend the application of machine learning to the study of frustrated spin systems without analytical solution and with continuous degrees of freedom;
- Intereaction with experimental groups to test the data analysis pipeline proposed to real world systems which are poorly understood;
- Analyse systems with a wider variety of behaviors, combining both second and first order phase transistions;

8.3 Publications

The works presented in this thesis has lead to the following publication:

- D. Elias, E. Granato and M. de Koning. *"Global exploration of phase behavior*

in frustrated Ising models using unsupervised learning techniques. Physica A, 589, 126653 (2022).

Bibliography

[1] Krauth, W. *Statistical Mechanics: Algorithms and Computations* (Oxford University Press, Oxford, 2006).

[2] Newman, M. & Barkema, G. *Monte Carlo Methods in Statistical Physics* (Clarendon Press, 1999). URL https://books.google.com.br/books?id=KKL2nQEACAAJ.

[3] Wolff, U. Critical slowing down. *Nucl. Phys. B Proc. Suppl.* **17**, 93–102 (1990). URL http://www.sciencedirect.com/science/article/pii/092056329090224I.

[4] Goldenfeld, N. *Lectures On Phase Transitions And The Renormalization Group* (CRC Press, 2018). URL https://books.google.com.br/books?id=HQpQDwAAQBAJ.

[5] Le Bellac, M., Mortessagne, F. & Batrouni, G. G. *Equilibrium and Non-Equilibrium Statistical Thermodynamics* (Cambridge University Press, 2004).

[6] Ising, E. Beitrag zur Theorie des Ferromagnetismus. *Zeitschrift fur Physik* **31**, 253–258 (1925).

[7] BRUSH, S. G. History of the lenz-ising model. *Rev. Mod. Phys.* **39**, 883–893 (1967). URL https://link.aps.org/doi/10.1103/RevModPhys.39.883.

[8] Onsager, L. Crystal statistics. i. a two-dimensional model with an order-disorder transition. *Phys. Rev.* **65**, 117–149 (1944). URL https://link.aps.org/doi/10.1103/PhysRev.65.117.

[9] URL https://indico.ictp.it/event/8644/session/48/contribution/112/material/slides/0.pdf.

[10] URL https://aapt.scitation.org/doi/10.1119/1.4868949.

[11] LESNE, A. & Laguës, M. *Scale Invariance: From Phase Transitions to Turbulence* (Springer Berlin Heidelberg, 2011). URL https://books.google.com.br/books?id=3p5hlEqfLOYC.

[12] URL https://www.researchgate.net/figure/Kadanoffs-decimation-and-renormalizatio fig10_322749680.

[13] URL https://www.tudelft.nl/tnw/over-faculteit/afdelingen/quantum-nanoscience/thijssen-group/education.

[14] Mattis, D. *The Theory of Magnetism Made Simple: An Introduction to Physical Concepts and to Some Useful Mathematical Methods*. The Theory of Magnetism Made Simple: An Introduction to Physical Concepts and to Some Useful Mathematical Methods (World Scientific, 2006). URL https://books.google.com.br/books?id=VkNBAQAAIAAJ.

[15] André, G., Bidaux, R., Carton, J.-P., Conte, R. & de Seze, L. Frustration in periodic systems : exact results for some 2d ising models. *J. Phys. France* **40**, 479–488 (1979). URL https://doi.org/10.1051/jphys:01979004005047900.

[16] Rodrigues de Assis Elias, D., Granato, E. & de Koning, M. Global exploration of phase behavior in frustrated ising models using unsupervised learning techniques. *Physica A: Statistical Mechanics and its Applications* **589**, 126653 (2022). URL https://www.sciencedirect.com/science/article/pii/S037843712100892X.

[17] Wolf, W. P. The ising model and real magnetic materials. *Brazilian Journal of Physics* **30** (2000). URL https://doi.org/10.1590/S0103-97332000000400030.

[18] URL https://en.wikipedia.org/wiki/Spin_ice.

[19] Bishop, C. M. *Pattern Recognition and Machine Learning*. Information Science and Statistics (Springer, 2006). URL https://books.google.com.br/books?id=kTNoQgAACAAJ.

[20] Goodfellow, I., Bengio, Y. & Courville, A. *Deep Learning*. Adaptive Computation and Machine Learning series (MIT Press, 2016). URL https://books.google.com.br/books?id=Np9SDQAAQBAJ.

[21] URL http://yann.lecun.com/exdb/mnist/.

[22] URL http://www.astroml.org/astroML-notebooks/chapter9/astroml_chapter9_Deep_Learning_Classifying_Astronomical_Images.html.

[23] URL https://optimal.uva.nl/project-plan/project-plan.html?cb.

[24] URL https://medium.com/datadl-ai/mnist-exploration-to-execution-25136ca00570.

[25] URL https://towardsdatascience.com/autoencoders-vs-pca-when-to-use-which-73de0

[26] URL https://www.deeplearningbook.com.br/introducao-aos-autoencoders/.

[27] URL https://iagml.github.io/blog/2020/10/image-denoising.

[28] URL https://scikit-learn.org/stable/modules/clustering.html.

[29] URL https://en.wikipedia.org/wiki/DBSCAN.

[30] Carrasquilla, J. & Melko, R. G. Machine learning phases of matter. *Nat. Phys.* **13**, 431 (2017). URL https://doi.org/10.1038/nphys4035.

[31] Carleo, G. *et al.* Machine learning and the physical sciences. *Rev. Mod. Phys.* **91**, 045002 (2019). URL https://link.aps.org/doi/10.1103/RevModPhys.91.045002.

[32] Hu, W., Singh, R. R. P. & Scalettar, R. T. Discovering phases, phase transitions, and crossovers through unsupervised machine learning: A critical examination. *Phys. Rev. E* **95**, 062122 (2017). URL https://link.aps.org/doi/10.1103/PhysRevE.95.062122.

[33] Casert, C., Vieijra, T., Nys, J. & Ryckebusch, J. Interpretable machine learning for inferring the phase boundaries in a nonequilibrium system. *Phys. Rev. E* **99**, 023304 (2019). URL https://link.aps.org/doi/10.1103/PhysRevE.99.023304.

[34] Acevedo, S., Arlego, M. & Lamas, C. A. Phase diagram study of a two-dimensional frustrated antiferromagnet via unsupervised machine learning. *Phys. Rev. B* **103**, 134422 (2021). URL https://link.aps.org/doi/10.1103/PhysRevB.103.134422.

[35] Wang, L. Discovering phase transitions with unsupervised learning. *Phys. Rev. B* **94**, 195105 (2016). URL https://link.aps.org/doi/10.1103/PhysRevB.94.195105.

[36] Ch'ng, K., Carrasquilla, J., Melko, R. G. & Khatami, E. Machine learning phases of strongly correlated fermions. *Phys. Rev. X* **7** (2017).

[37] Ponte, P. & Melko, R. G. Kernel methods for interpretable machine learning of order parameters. *Phys. Rev. B* **96** (2017). URL https://doi.org/10.1103/PhysRevB.96.205146.

[38] Nieuwenburg, E. P. L., Liu, Y.-H. & Huber, S. D. Learning phase transitions by confusion. *Nat. Phys.* **13** (2017). URL https://doi.org/10.1038/nphys4037.

[39] Deng, D. L., Li, X. & Sarma, S. Machine learning topological states. *Phys. Rev. B* **96** (2017). URL https://doi.org/10.1103/PhysRevB.96.195145.

[40] Wetzel, S. J. Unsupervised learning of phase transitions: From principal component analysis to variational autoencoders. *Phys. Rev. E* **96**, 022140 (2017). URL https://link.aps.org/doi/10.1103/PhysRevE.96.022140.

[41] Wetzel, S. J. & Scherzer, M. Machine learning of explicit order parameters: from the ising model to su(2) lattice gauge theory. *Phys. Rev. B* **96** (2017). URL https://doi.org/10.1103/PhysRevB.96.184410.

[42] Ch'ng, K., Vazquez, N. & Khatami, E. Unsupervised machine learning account of magnetic transitions in the hubbard model. *Phys. Rev. E* **97** (2018). URL https://doi.org/10.1103/PhysRevE.97.013306.

[43] Liu, Y.-H. & van Nieuwenburg, E. P. L. Discriminative cooperative networks for detecting phase transitions. *Phys. Rev. Lett.* **120**, 176401 (2018). URL https://link.aps.org/doi/10.1103/PhysRevLett.120.176401.

[44] Nieuwenburg, E., Bairey, E. & Refael, G. Learning phase transitions from dynamics. *Phys. Rev. B* **98** (2018). URL https://doi.org/10.1103/PhysRevB.98.060301.

[45] Kim, D. & Kim, D.-H. Smallest neural network to learn the ising criticality. *Phys. Rev. E* **98**, 022138 (2018). URL https://link.aps.org/doi/10.1103/PhysRevE.98.022138.

[46] Mills, K. & Tamblyn, I. Deep neural networks for direct, featureless learning through observation: The case of two-dimensional spin models. *Phys. Rev. E* **97**, 032119 (2018). URL https://link.aps.org/doi/10.1103/PhysRevE.97.032119.

[47] Venderley, J., Khemani, V. & Kim, E.-A. Machine learning out-of-equilibrium phases of matter. *Phys. Rev. Lett.* **120**, 257204 (2018). URL https://link.aps.org/doi/10.1103/PhysRevLett.120.257204.

[48] Ceriotti, M. Unsupervised machine learning in atomistic simulations, between predictions and understanding. *J. Chem. Phys.* **150**, 150901 (2019). URL https://doi.org/10.1063/1.5091842.

[49] Rodriguez-Nieva, J. F. & Scheurer, M. S. Identifying topological order through unsupervised machine learning. *Nat. Phys.* **15**, 790–795 (2019). URL https://doi.org/10.1038/s41567-019-0512-x.

[50] Freitas, R. & Reed, E. J. Uncovering the effects of interface-induced ordering of liquid on crystal growth using machine learning. *Nat. Commun.* **11**, 3260 (2020). URL https://doi.org/10.1038/s41467-020-16892-4.

[51] Wang, C. & Zhai, H. Machine learning of frustrated classical spin models. i. principal component analysis. *Phys. Rev. B* **96**, 144432 (2017). URL https://link.aps.org/doi/10.1103/PhysRevB.96.144432.

[52] Wang, C. & Zhai, H. Machine learning of frustrated classical spin models (ii): Kernel principal component analysis. *Front Phys-beijing* **13**, 130507 (2018). URL https://doi.org/10.1007/s11467-018-0798-7.

[53] Théveniaut, H. & Alet, F. Neural network setups for a precise detection of the many-body localization transition: Finite-size scaling and limitations. *Phys. Rev. B* **100**, 224202 (2019). URL https://link.aps.org/doi/10.1103/PhysRevB.100.224202.

[54] Alexandrou, C., Athenodorou, A., Chrysostomou, C. & Paul, S. The critical temperature of the 2d-ising model through deep learning autoencoders. *Eur. Phys. J. B* **93**, 226 (2020). URL https://doi.org/10.1140/epjb/e2020-100506-5.

[55] Purnomo, H. D., Wahyono, T. & Heryadi, Y. Machine learning applications for anomaly detection. 49–83 (IGI Global, Hershey, PA, USA, 2019). URL https://services.igi-global.com/resolvedoi/resolve.aspx?doi=10.4018/978-1-5225-7955-7.ch003.

[56] Villain, J. Spin glass with non-random interactions. *J. Phys. C: Solid State Phys.* **10**, 1717–1734 (1977). URL http://dx.doi.org/10.1088/0022-3719/10/10/014.

[57] Newman, M. E. J. & Barkema, G. T. *Monte Carlo Methods in Statistical Physics* (Oxford University Press, 1999). URL https://books.google.com.br/books?id=J5aLdDN4uFwC.

[58] Murphy, K. P. *Machine Learning: A Probabilistic Perspective*. Adaptive Computation and Machine Learning series (MIT Press, 2012). URL https://books.google.com.br/books?id=NZP6AQAAQBAJ.

[59] Estivill-Castro, V. Why so many clustering algorithms: A position paper. *SIGKDD Explor. Newsl.* **4**, 65–75 (2002). URL https://doi.org/10.1145/568574.568575.

[60] Pedregosa, F. *et al.* Scikit-learn: Machine learning in Python. *J. Mach. Learn. Res.* **12**, 2825–2830 (2011).

[61] Pearson, K. Liii. on lines and planes of closest fit to systems of points in space. *Phil. Mag. Series 6* **2**, 559–572 (1901). URL https://doi.org/10.1080/14786440109462720.

[62] Jolliffe, I. T. *Principal Component Analysis*. Springer Series in Statistics (Springer New York, 2006). URL https://books.google.com.br/books?id=6ZUMBwAAQBAJ.

[63] Kramer, M. A. Nonlinear principal component analysis using autoassociative neural networks. *AIChE J.* **37**, 233–243 (1991). URL https://doi.org/10.1002/aic.690370209.

[64] Ester, M., Kriegel, H.-P., Sander, J. & Xu, X. In Simoudis, E., Han, J. & Fayyad, U. (eds.) *Proceedings of the Second International Conference on Knowledge Discovery and Data Mining*, 226 (AAAI, Palo Alto, 1996).

[65] Rahmah, N. & Sitanggang, I. S. Determination of optimal epsilon (eps) value on dbscan algorithm to clustering data on peatland hotspots in sumatra. *IOP Conf. Ser.: Earth Environ. Sci.* **31**, 012012 (2016). URL http://dx.doi.org/10.1088/1755-1315/31/1/012012.

[66] Cortes, C. & Vapnik, V. Support-vector networks. *Mach. Learn.* **20**, 273–297 (1995). URL https://doi.org/10.1007/BF00994018.

[67] Paszke, A. *et al.* Pytorch: An imperative style, high-performance deep learning library. In Wallach, H. *et al.* (eds.) *Advances in Neural Information Processing Systems 32*, 8024–8035 (Curran Associates, Inc., 2019). URL http://papers.neurips.cc/paper/9015-pytorch-an-imperative-style-high-performance-deep-learning-library.pdf.

[68] Davidson, T. R., Falorsi, L., Cao, N. D., Kipf, T. & Tomczak, J. M. Hyperspherical variational auto-encoders. In *Proceedings of the Thirty-Fourth Conference on Uncertainty in Artificial Intelligence, UAI 2018, Monterey, California, USA, August 6-10, 2018*, 856–865 (2018). URL http://auai.org/uai2018/proceedings/supplements/Supplementary-Paper309.pdf.

[69] Joshi, M. R. & Patil, Y. S. Analysis of change in coordinate system on clustering. In *2016 IEEE International Conference on Current Trends in Advanced Computing (ICCTAC)*, 1–7 (2016).

[70] Patil, Y. S. & Joshi, M. R. Clustering with polar coordinates system: Exploring possibilities. In *Smart Intelligent Computing and Applications*, 553–560 (Springer Singapore, Singapore, 2019).

[71] Kiwata, H. Deriving the order parameters of a spin-glass model using principal component analysis. *Phys. Rev. E* **99**, 063304 (2019). URL https://link.aps.org/doi/10.1103/PhysRevE.99.063304.

[72] Kottmann, K., Huembeli, P., Lewenstein, M. & AcÃn, A. Unsupervised phase discovery with deep anomaly detection. *Phys. Rev. Lett.* **125**, 170603 (2020). URL https://link.aps.org/doi/10.1103/PhysRevLett.125.170603.